Effect of short-range ordering and grain boundary segregation on shear deformation of CoCrFeNi high-entropy alloys with Al addition

Rita Babicheva [a], Asker Jarlöv [a b], Han Zheng [c], Sergey Dmitriev [d e], Elena Korznikova [d f], Mui Ling Sharon Nai [b], Upadrasta Ramamurty [a], Kun Zhou [a c]

[a] School of Mechanical and Aerospace Engineering, Nanyang Technological University, 50 Nanyang Avenue, Singapore 639798, Singapore

[b] Singapore Institute of Manufacturing Technology, 73 Nanyang Drive, Singapore 637662, Singapore

[c] Environmental Process Modelling Centre, Nanyang Environment and Water Research Institute, Nanyang Technological University, 1 Cleantech Loop, Singapore 637141, Singapore

[d] Institute of Molecule and Crystal Physics, Ufa Federal Research Centre of the Russian Academy of Sciences, Oktyabrya Ave. 151, Ufa 450075, Russia

[e] Center for Design of Functional Materials, Bashkir State University, Zaki Validi St. 32, Ufa 450076, Russia

[f] Ufa State Aviation Technical University, Karl Marx St. 12, Ufa 450077, Russia

Abstract

A method combining molecular dynamics (MD) and Monte Carlo (MC) simulation is used to analyze the short-range ordering and grain boundary (GB) segregation in the bi-crystals of equiatomic CoCrFeNi and Al (8 at%)-CoCrFeNi high-entropy alloys (HEAs). Based on the structures of the two HEAs obtained by the combined MC/MD method, their defect evolution and deformation mechanisms during shear deformation at 300 K are studied. In addition, the bi-crystals of the Al (8 at%)-CoCrFeNi HEA with the inclusion of B2 intermetallic AlNi particles at the GBs are considered. For the CoCrFeNi HEA, the Cr and Fe atoms are revealed to segregate to GBs. In contrast, it is observed in the Al (8 at%)-CoCrFeNi HEA that Al and Fe have a strong tendency to segregate to GBs, while local ordering results in the formation of Fe_3Al clusters, which in turn increase the stacking fault energy of the alloy. The GB segregation and the deformation behaviour of the alloys are found to be highly sensitive to the crystallographic orientation of the bi-crystals. The GB segregation, especially by the Al atoms, stabilizes the GBs and resists the plastic deformation through GB sliding and the GB migration. Overall, the Al (8 at%)-CoCrFeNi

HEA with Al-atom segregation at GBs demonstrates an increased shear yield strength compared with the material without the Al addition. On the other hand, the AlNi particles reduce the yield strength of the HEA owing to the formation of amorphous structure at the face-centered cubic/B2 interface and thus facilite the GB sliding. The obtained results provide insights into designing HEAs with improved mechanical properties through GB engineering.

Graphical abstract

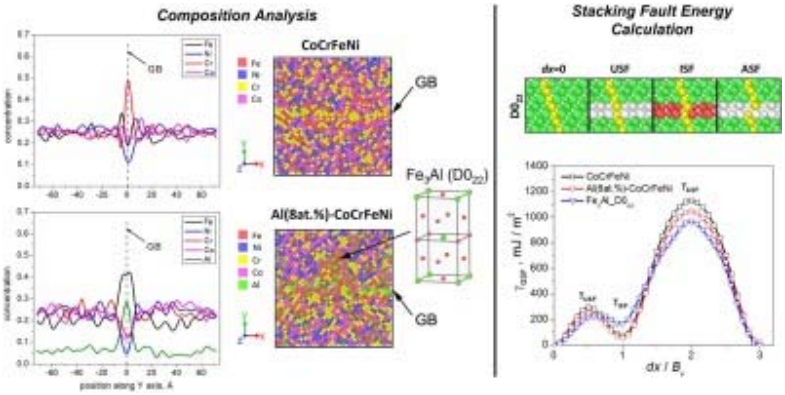

Download: Download high-res image (274KB)
Download: Download full-size image

Keywords

High-entropy alloy; Molecular dynamics simulation; Monte-Carlo simulation; Grain boundary segregation; Local ordering; Deformation mechanism

1. Introduction

Multi-element high-entropy alloys (HEAs) have garnered increasing research attention since their introduction in 2004 [1], [2]. Their unique features, such as high specific entropy, slow diffusion, and strong lattice distortion [2], [3], can lead to enhanced physical properties (e.g., thermal conductivity, electrical conductivity, and radiation resistance) and mechanical properties (e.g., crack resistance, hardness, elastic modulus, strength, and ductility) [4], [5], [6] that are crucial in advanced engineering applications.

There are several well-known examples of CoCrFeNi-based HEAs demonstrating improved mechanical properties with Al doping. For example, the $Al_{0.5}$CoCrCuFeNi alloy showed high fatigue resistance [7], and AlCoCrFeNiTi-based alloys exhibited high wear resistance [8]. In [9], it was shown that Al doping can drastically reduce the crack density in the solidified material obtained by additive manufacturing, while the authors of [10] reported on both the improved strength and ductility of a nano-lamellar $AlCoCrFeNi_{2.1}$ alloy.

The equiatomic CoCrFeNi Cantor alloy has the face-centered cubic (fcc) structure. However, it was shown both experimentally and theoretically that depending on the Al content and the temperature, the crystal structure of the Al_xCoCrFeNi HEA can be either fcc, body-centered cubic (bcc), or a combination of both. In [11], the authors estimated the phase stability of multiple HEAs with different Al concentrations and reported that by increasing the Al content above 13.4 at% ($x \sim 0.62$), the fcc to bcc phase transition occurred. A similar conclusion was made in [12], where an fcc structure could be observed when x was smaller than 0.5, a mixture of the fcc and bcc phases was formed when the Al content was in the range of 0.5–0.9, and a single bcc phase was formed when x was larger than 0.9. However, the authors of [13] found that the fcc–bcc mixture could be observed when $0.6 < x < 1.23$.

In general, it has been assumed that the distribution of elements within HEAs is random to maximize the entropy [14]. However, recent studies provide strong evidence that this assumption is not entirely true. HEAs can demonstrate local ordering, forming various intermetallic compounds and elemental segregation to lattice defects which strongly affect the properties of such alloys. It is believed that the segregation of Al, Ni, and Co atoms in Al_xCoCrFeNi alloys can lead to the formation of the B2 phase due to the negative formation enthalpy for Al–Co and Al–Ni bonds (close to –60 kJ mol^{-1}) [15], [16]. It was shown experimentally in [13] that in the $Al_{0.75}$CoCrFeNi HEA, the fcc matrix phase was enriched with Fe, Cr, and Co atoms, while the B2 phase was enriched with Al and Ni atoms. Significant segregation of Cr and Al atoms to the fcc and formed B2 phases, respectively, was demonstrated. The tendency to form AlNi compounds with B2 lattice during solidification after laser powder bed fusion was also revealed in [9]. The authors found that the Al atoms partitioned into the interdendritic regions and segregated to the GBs of the $Al_{0.5}$CoCrFeNi HEA, resulting in the formation of ordered AlNi compounds and disordered bcc phases enriched in Cr via spinodal decomposition.

Both equilibrium and non-equilibrium segregation is possible due to thermodynamic and kinetic processes, respectively. The earlier examples represented equilibrium segregation. The authors of [17] revealed that deformation-induced non-equilibrium segregation of Al

occurred at GBs and interfaces during superplastic deformation (at 800 °C and under a strain rate of 5×10^{-2} s^{-1}) of the $Al_{0.3}$CoCrNi HEA. The superplastic deformation resulted in the formation of a thin film of the liquid Al phase, rationalized by an excess of supersaturated vacancy complexes and a tendency of solute atoms to form secondary phases.

It is believed that GB segregation and the formation of intermetallic phases through local ordering can alter the mechanical properties and deformation mechanisms of HEAs. Using atom probe tomography, it has been found that nanoclusters of Cr, Ni, and Mn located at GBs of the CoCrFeMnNi HEA reduce GB cohesion and promote crack initiation, thus reducing the ductility [18]. The CoCrFeMnNi HEA subjected to deformation followed by annealing was examined in [19], [20]. It was found that Cr atoms segregated to individual dislocations and that the Cr-rich σ phase precipitated at GBs and shear bands. The segregation and precipitation effectively suppressed the grain growth by GB pinning, resulting in a fine-grained microstructure. The authors attributed the high strength of the material to precipitation strengthening. Due to the poor ductility of the Al- and Ni-rich B2 phase, the ductility of the Al_xCoCrFeNi HEAs can be substantially reduced [13]. However, it was reported in [9] that interdendritic/GB microstructure containing the AlNi phase helped reduce the crack density in the $Al_{0.5}$CoCrFeNi HEA.

Along with experimental studies, there are several works devoted to local ordering and segregation in HEAs based on theoretical approaches. Since the formation of such structural elements occurs at the atomic scale, the investigation of short-range ordering and clustering in metallic materials using molecular dynamics (MD) and Monte Carlo (MC) simulations becomes more popular. In [21], the interaction of interstitials with lattice defects was examined by comparing the results of the random CoCuFeNi HEA and the equilibrated HEA with local ordering, which were obtained through atomistic simulations using both the MC and MD methods. It was shown that short-range ordering of the equilibrated HEA resulted in the significant segregation of Cu atoms near the GBs and the formation of non-fcc regions in the considered bi-crystals. Such segregation can enhance the sink strength of the GBs for vacancies and reduce it for interstitials. The accumulation of Cu atoms in the vicinity of GBs in the CoCuNiFe HEA was also detected using the hybrid MC/MD method in [22]. Solute segregation to GBs in HEAs suppresses GB migration and may hinder grain growth in fcc HEAs. Using MC, MD, and lattice statics methods, the authors of [23] studied the formation of surface and GB segregation in the equiatomic CoCrFeMnNi HEA. They found that Cr atoms were the dominant segregant at GBs, while the segregation of Mn atoms was stronger at the surface. By using the hybrid MC/MD approach, a strong local ordering of Al and Fe atoms was also revealed in the Al_xCoCrFeNi HEA [24].

The atom type as well as GB characteristics (i.e., the misorientation angle between grains, the Σ value, GB energy, and free volume) strongly affect interactions among elements at GBs [25], [26], [27] and the deformation behaviour of the material [28], [29], [30]. However, due to the compositional complexity of the HEAs, current experimental and theoretical studies do not offer a clear understanding of the effects of GB segregation and intermetallic phases on the deformation mechanisms and mechanical behaviour of the HEAs with Al addition. The primary objective of the current study is thus to understand the interactions of the constituent elements with each other and with GBs, with a

particular emphasis on their tendency to form local ordering and/or GB segregation in equiatomic CoCrFeNi HEAs with and without Al addition, based on the hybrid MC/MD simulation. Additionally, the effect of the formed microstructures, with and without B2 inclusions, on the deformation mechanisms during shear loading at room temperature (300 K) are analyzed by using MD simulation.

2. Methodology

In practice, the formation of GB segregation in metallic alloys can be observed when they are cooled from a high temperature and subsequently held at a lower temperature for a period of time. As for HEAs fabricated by, for example, the laser powder bed fusion technique, such segregation is formed during the solidification process. Thus, it is believed that with decreasing temperature during the solidification, the solubility of Al in the fcc matrix of CoCrFeNi HEA alloys reduces, resulting in its partitioning into the interdendritic regions and formation of GB segregation [9]. Unfortunately, atomistic simulations cannot capture the solidification process of HEAs due to their limited spatial and temporal scales. Therefore, MC simulation is widely used to mimic the final distribution of atoms in the structure at a certain temperature [21], [23], [24].

To obtain the steady-state structures with possible GB segregation, the hybrid MC/MD modeling is performed for two different HEAs, namely, the quaternary equiatomic CoCrFeNi HEA with and without Al addition, through simultaneous MC atom swaps and MD thermalization until the minimum energy is reached. Further, for modeling the shear deformation process at room temperature, the MD simulation with computational cells constructed based on the swapped models is performed.

Both the MD and hybrid MC/MD simulations are conducted by utilizing the large-scale atomic/molecular massively parallel simulator (LAMMPS) program package [31]. The interatomic forces in the considered systems are described by the many-body embedded-atom method (EAM) potential developed by D. Farkas and A. Caro [24] based on their previous work [32]. This EAM potential can capture the effects of Al addition on the CoCrFeNi HEAs. For instance, with an increase in the Al content, the average lattice parameter increases and the ordered B2 phase becomes more stable. The authors concluded that the ability to predict the stability of fcc quinary mixtures and ordered $L1_2$ and B2 phases as a function of the Al content were in qualitative agreement with experiments.

The deformation mechanisms and effect of GB segregation in polycrystalline materials cannot be interpreted unambiguously, and the deformation behaviour in such materials is most appropriately studied for specific flat GBs with a defined geometry. Therefore, the hybrid MC/MD modeling and the shear deformation simulation are performed on bi-crystalline samples with tilt GBs. For visualization of the atomic structures, the Open Visualization Tool (OVITO) software [33] is adopted.

2.1. Hybrid MC/MD simulation

To reach a steady-state condition and to reveal the tendency of elemental GB segregation, hybrid MC/MD modeling is performed for two different materials, namely the quaternary equiatomic CoCrFeNi and quinary Al (8 at%)-CoCrFeNi HEAs, hereafter referred to as M1 and M2, respectively. As we are interested in the HEA with the fcc structure, the Al content is set to 8 at% ($Al_{0.45}$CoCrFeNi), at which a stable fcc matrix is observed [11], [12], [13]. It is believed that the HEA with the selected composition demonstrates enhanced plasticity [34] and high resistance to crack formation during laser powder bed fusion [9], [35]. To model the short-range ordering and obtain materials

with GB segregation in various HEAs, a similar MC procedure has been applied in several recent works [21], [23], [24].

Four different computational cells with dimensions of about 17.0 nm × 22.0 nm × 0.7 nm are constructed by using the Atomsk [36] and OVITO software. The cells are filled with about 20,000 atoms, and the four (for M1) or five (for M2) different elements are randomly distributed on fcc crystal sites.

Fig. 1 shows two of the four computational cells used for the simulation. Two tilt GBs exist in each computational cell, both being parallel to the *xz*-plane. The first tilt GB is exactly in the middle of the cells, while the other is formed by the upper and lower faces of the simulation cells. The GBs are introduced by rotating the initial lattice with crystallographic orientations given in Fig. 1 about the *z*-axis. For O1 the *z*-axis is parallel to the [001] crystallographic direction, while for O2 it is parallel to the [$11\bar{2}0$] direction. The rotation angles $\alpha 1$ and $\alpha 2$ with the same magnitude but opposite sign are applied to grains 1 and 2, respectively. Such a procedure results in the formation of symmetrical and non-symmetrical tilt GBs in O1 and O2, respectively. Two different misorientation angles θ between grains 1 and 2 are considered for each crystallographic orientation, $\theta = 30°$ ($\alpha 1 = +15°$, $\alpha 2 = -15°$) and $\theta = +70°$ ($\alpha 1 = +35°$, $\alpha 2 = -35°$). In total, four different bi-crystals are created, hereafter denoted as O1_30, O2_30, O1_70, and O2_70 depending on the initial orientation of the lattice and misorientation angle.

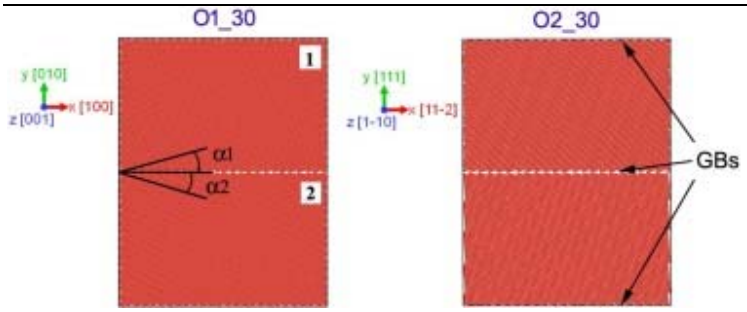

1. Download: Download high-res image (214KB)
2. Download: Download full-size image

Fig. 1. Computational cells O1_30 and O2_30 used for the hybrid MC/MD simulation.

Prior to the MC swapping, the obtained bi-crystals with the constituent elements randomly distributed within the samples are subjected to energy minimization by the conjugate gradient method and further equilibrated at room temperature (300 K) in the NPT (constant number of atoms, pressure, and temperature) ensemble for 50 ps while the pressure components are kept at 0 Pa. During this step, the periodic boundary conditions are applied along the three orthogonal directions of the cells. The timestep is set to 1 fs.

It should be noted that in the current work, the GB structure with the global energy minimum was not considered. It is believed that for obtaining a more realistic GB structure, it is important to apply a rigid-body translation method [37] before the energy minimization to find the global energy minimum. However, the preliminary test simulations showed that the mechanical response of M1 before the MC modeling for the

bi-crystals with a local and global energy minimum is consistent and dictated by the same deformation mechanisms.

The MC swapping procedure is carried out with simultaneous regular MD time integration displacement steps using the NPT ensemble at 300 K without normal or shear stresses for the structure to reach a steady-state condition with reduced energy. The MC swapping of atoms of one type with atoms of another type follows the Metropolis acceptance criterion [38] that dictates atom swap probabilities at a certain temperature. The $i+1^{th}$ MC swap is accepted if the energy of the HEA after the attempt, E_{i+1}, is lower than that calculated at the previous swap, E_i. Otherwise, it is accepted with the probability

$$P = e^{\frac{E(i+1)-E(i)}{kT}}, \quad (1)$$

where k is the Boltzmann constant and T is the temperature. The MC swap is accepted when a random number R, uniformly generated within the interval (0, 1), is smaller than or equal to P. The kinetic energy of each atom is kept the same before and after the swap. In every timestep, three atom swaps are invoked. For M1 without Al addition, the atoms undergo a total of 210,000 swaps; while for M2 with Al addition, the initially high energy configuration of the system increases the number of swaps to 600,000 because of the significant lattice distortion caused by the large Al atoms [24]. The simultaneous MD simulation in the NPT ensemble is conducted for 70 and 200 ps, respectively.

The chemical affinity among the constituent elements in M1 and M2 can be assessed through the calculation of the Warren–Cowley parameters (WCPs) for different atomic pairs at the first nearest neighbour shell using

$$WCP_{mn} = 1 - Z_{mn} / (\chi_n Z_m), \quad (2)$$

where Z_{mn} is the number of n-type atoms around m-type atoms, Z_m is the total number of atoms around m-type atoms, and χ_n is the atomic fraction of n-type atoms in the HEA [39]. When WCP_{mn} equals 0, the m–n atomic pairs are distributed randomly without any ordering. If WCP_{mn} is greater than 0, such pairs can be found in the material less often than if they are distributed randomly; while when WCP_{mn} is smaller than 0, the chemical bonding between n- and m-type atoms is more favourable. A similar analysis for the description of the local ordering in HEAs was utilized in several recent works [40], [41].

2.2. Shear deformation modeling setup

Unlike the hybrid MC/MD modeling where only two materials with different chemical compositions are subjected to the swapping procedure, simulation of the shear deformation considers materials with three different compositions. These materials include the quaternary equiatomic CoCrFeNi HEA, the quinary Al (8 at%)-CoCrFeNi HEA, and the material with AlNi B2 intermetallic inclusions at GBs of the M2 model, in which the Al content is changed from the initial 8 at% to 6 at% and 5 at% in the fcc matrix and B2 intermetallics, respectively (i.e., Al (6 at%)-CoCrFeNi–AlNi (10 at%)). Hereafter, these alloys are denoted as M1, M2, and M3, respectively.

The computational cells for the shear deformations are created based on the swapped structures through their replication in the *z*-direction to increase the cell dimensions (about 22.0 nm × 17.0 nm × 3.0 nm). The total number of atoms in each simulation cell after such a procedure is about 75,000.

The strain-controlled shear loading is performed in the NPT ensemble at 300 K, and the samples are deformed in the *xy*-plane with a shear strain γ up to 0.5 at a constant strain rate of 5×10^8 s^{-1}. Such a high strain rate is acceptable [42], [43], [44] considering the limited temporal scale of MD simulations. Preliminary test simulations using different strain rates (10^8–10^9 s^{-1}) for M1_O1_30 and M2_O1_30 proved that within the considered interval, the strain rate only slightly affects the stress–strain relation. During the deformation, the normal and shear stress components except τ_{xy} are controlled to be zero. Periodic boundary conditions are applied in all three orthogonal directions of the simulation cells.

3. Results

The results obtained from the MC/MD hybrid simulation that demonstrate the trend of local ordering and the tendency to form GB segregation in the considered HEA models with and without Al addition will be presented first. Afterwards, the shear deformation stress–strain relations and the deformation mechanisms for the considered structures, including those having B2 inclusions at the GBs, will be described and analyzed.

3.1. Hybrid MC/MD simulation

3.1.1. Energy minimization during hybrid MC/MD simulation

Fig. 2 demonstrates the decrease in energy during the hybrid MC/MD swapping procedure. The average energy per atom of both alloys in the considered models drops rapidly at the initial stage, which is especially evident for the material containing Al (M2), and then reaches an equilibrium state or a quasi-steady state in the case of M1 and M2 respectively. For the latter case, reaching a fully equilibrated state might require additional MC steps.

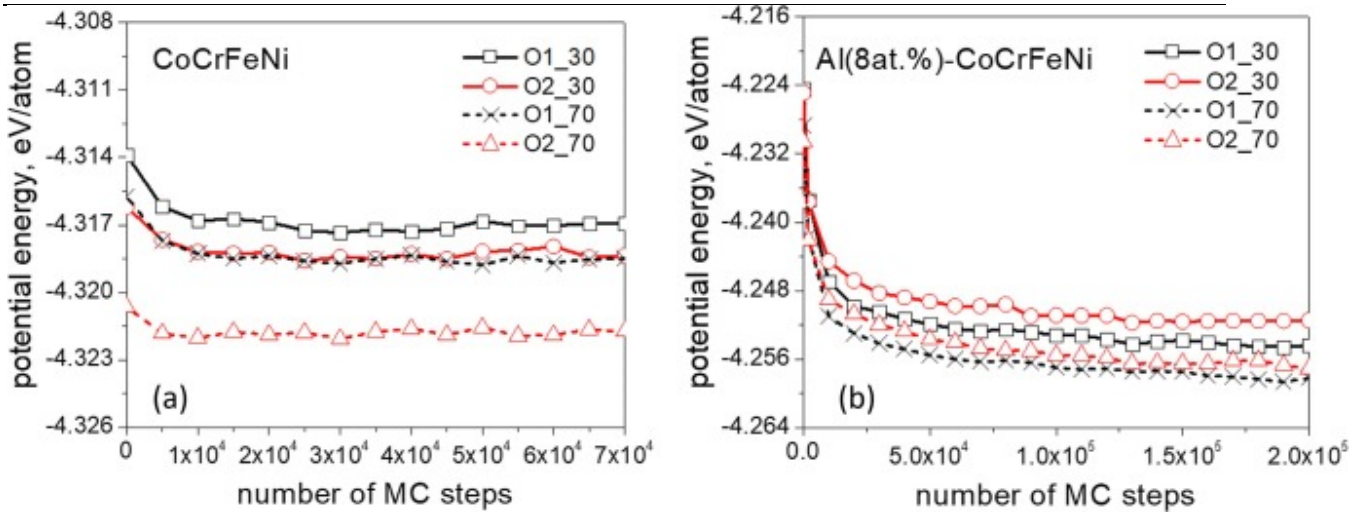

1. Download: Download high-res image (300KB)
2. Download: Download full-size image

Fig. 2. Decrease in the average energy per atom during hybrid MC/MD simulation for the considered models. MC swapping is performed at 300 K. In (a), the energy is given for the bi-crystals of M1, while the corresponding dependency for M2 is presented in (b).

It is clearly seen that the energy per atom in M2 before and after the MC/MD swapping procedure are considerably higher than those calculated for M1. Overall, the MC/MD equilibration approach affects the energy value very slightly for the material without Al (Fig. 2a), especially for sample O2_70, which initially has a low-energy configuration. In the case of the Al (8 at%)-CoCrFeNi HEA (Fig. 2b), the energy of the samples drops significantly during the simulation. It is observed that for the same material (M1 or M2) and initial crystallographic orientation (O1 or O2), the energy decreases with an increase in the misorientation angle between crystals

from θ = 30° to θ =70°. One major difference between M1 and M2 is that the energy per atom for bi-crystals of the O1 model is lower than that of the O2 model for M2 (with Al) while the opposite is true for M1 (without Al). This observation is true for both values of θ.

3.1.2. Short-range ordering

In Fig. 3, Fig. 4, the composition profiles calculated along the y-direction, which includes the GB at the center of each bi-crystal (y = 0 Å), are given for the different models after hybrid MC/MD swapping at 300 K to demonstrate the tendency for local ordering and GB segregation in the materials.

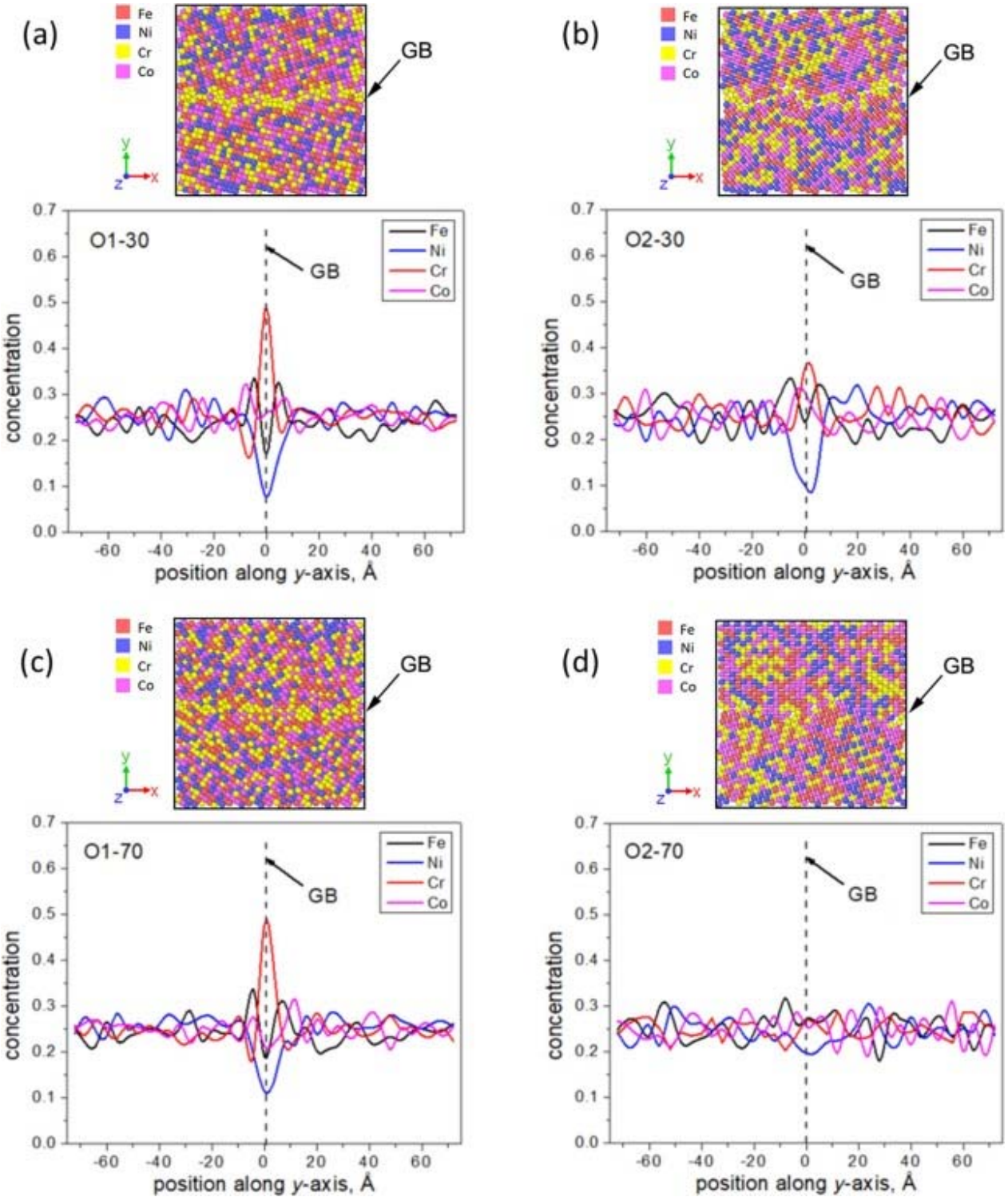

1. Download: Download high-res image (855KB)
2. Download: Download full-size image

Fig. 3. M1 composition profiles for (a) O1_30, (b) O2_30, (c) O1_70, and (d) O2_70 along the y-axis after the MC/MD swapping at 300 K. The position of the middle GB (at y = 0 Å)

is shown by the vertical dashed line. Above each composition profile, the corresponding atomic structure around the central GB is given.

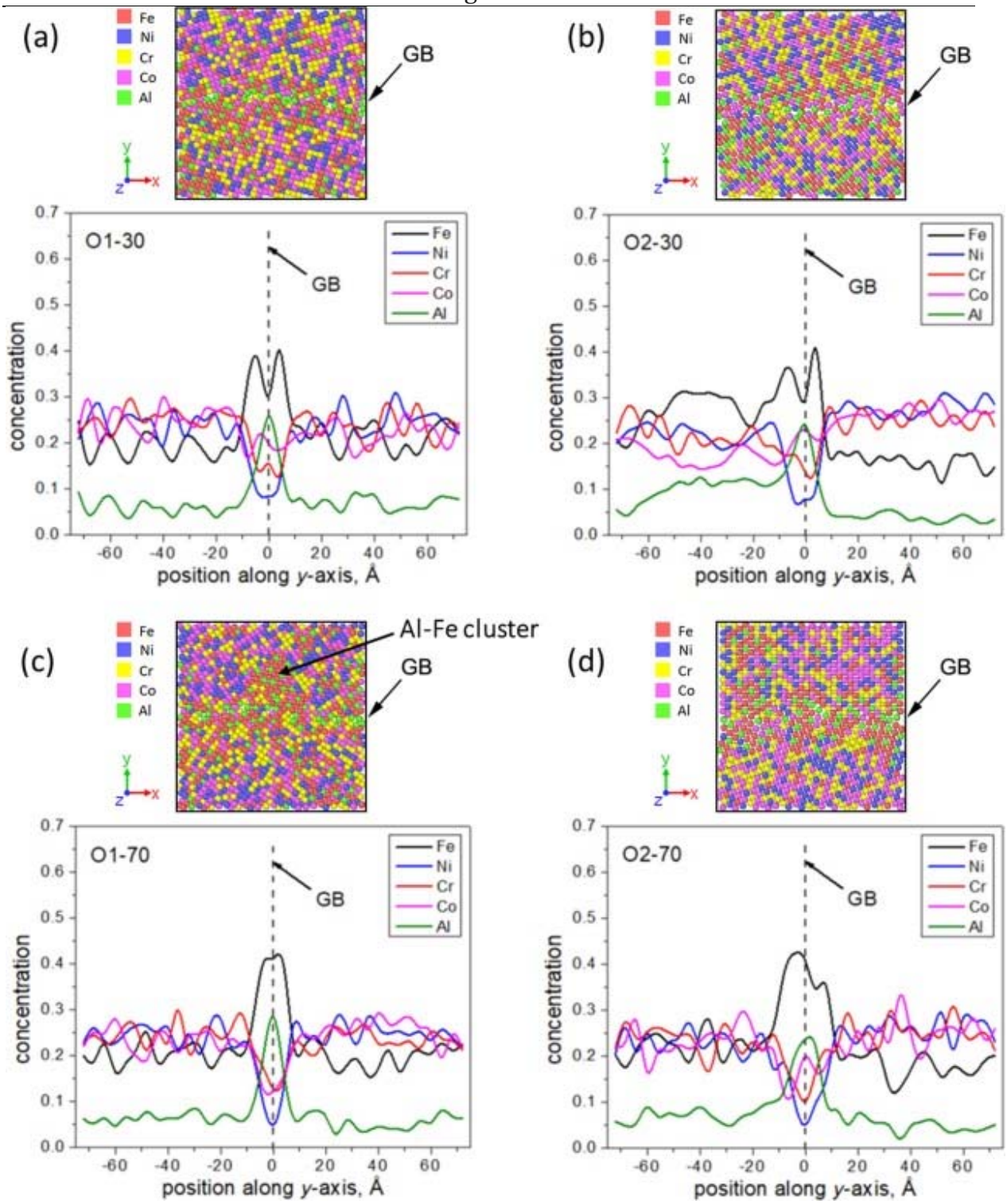

1. Download: Download high-res image (930KB)
2. Download: Download full-size image

Fig. 4. M2 composition profiles for (a) O1_30, (b) O2_30, (c) O1_70, and (d) O2_70 along the y-axis after the MC/MD swapping at 300 K. The position of the middle GB (at y = 0 Å) is shown by the vertical dashed line. Above each composition profile, the corresponding atomic structures around the central GB is given.

As can be seen from Figs. 3a and 3c, the HEA without Al demonstrates strong segregation of Cr atoms to the GBs for both O1 bi-crystals. The accumulation of Fe atoms surrounding the segregation results in the bimodal distribution in the composition profiles of Fe, with the minimum value appearing at y = 0 Å (GB area). However, this trend is not observed for O2 bi-crystals, especially when θ =70°. The GB segregation is suppressed in O2_30 (Fig. 3b) and cannot be observed in O2_70 (Fig. 3d). For all considered models, except O2_70, the MC/MD swapping results in a strong repulsion of Ni atoms from the GB regions.

In the case of the HEA with Al (M2), the segregation of the Cr atoms to the GBs is completely suppressed (Figs. 4a–4d). Similar to the Ni atoms, the Cr and Co atoms demonstrate a repulsion from the GB regions while the Al atoms show strong segregation to the GBs. This phenomenon is true for all bi-crystals, even for O2_70, for which the GB segregation was not observed in the case of M1. Similar to M1, the composition profile of Fe shows a bimodal distribution around the GB area, which is especially evident in models with a lower θ. It is important to note that along with the GB segregation of Al atoms that are randomly distributed within the GB area, the local ordering of Al and Fe at the GB regions and inside grains is shown after the hybrid MC/MD simulation, which results in the presence of Al–Fe clusters in the equilibrated samples (Fig. 4c). This is the reason why the bimodal shape of the composition profile for Fe becomes less obvious than that for the material without Al. The structure of the ordered phase will be considered in detail later. The formation of the Al–Fe clusters leads to the repulsion of other elements and a change in the local composition, which can be clearly seen from the difference in the profile level within grains, especially for O2_30. The tendency to form ordered clusters at GBs is slightly higher for O2 than for O1.

Fig. 5 presents the calculated WCPs for the bi-crystals M1_O1_30 and M2_O1_30 subjected to the MC swapping procedure. It is seen that for the HEA without Al (Fig. 5a), the WCPs for the different atomic pairs are very close to zero, indicating that the atoms in this material are randomly distributed. However, for M2 (Fig. 5b), a strong ordering of the Al and Fe atoms can be observed. Positive values for the Al–Al, Al–Ni, Al–Cr, Al–Co, Fe–Co, Fe–Cr, and Fe–Ni pairs are associated with the low chemical affinity among such atomic combinations. The parameters for the other atomic combinations are nearly zero, denoting their random distribution in the HEA.

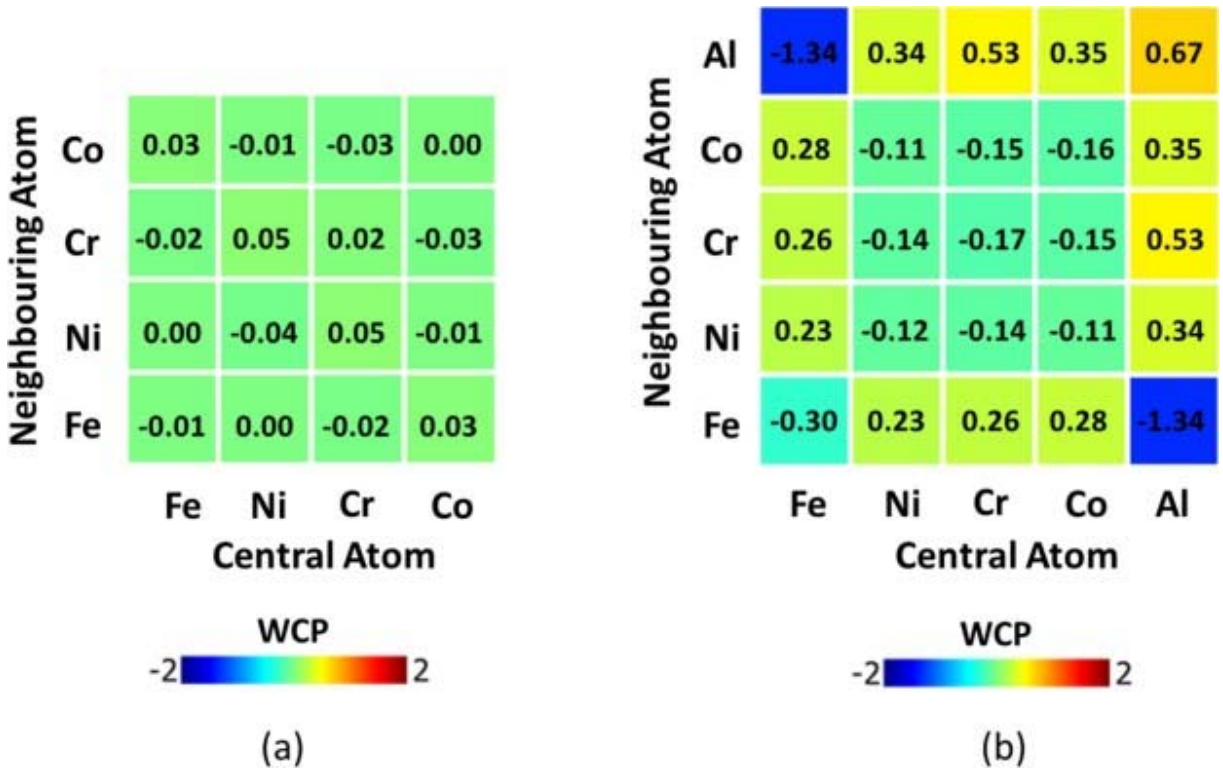

1. Download: Download high-res image (268KB)
2. Download: Download full-size image

Fig. 5. WCPs for the first nearest neighbour shell of all elemental pairs in the HEAs: M1 (a) and M2 (b) for the bi-crystal O1_30.

3.2. Shear deformation behaviour

3.2.1. Models for shear deformation simulation

Fig. 6 presents the 12 simulation cells used for the shear deformation. The models using different compositions (M1, M2, or M3), initial orientations (O1 or O2), and misorientation angles θ (30° or 70°) are presented. Recall that M1 does not include Al, M2 includes Al, and M3 includes Al in the fcc matrix and the AlNi intermetallic particles having B2 lattice at the GBs. The bi-crystals O1 have [001] as their misorientation axis, while for O2 the misorientation axis is $[11\bar{0}]$ (Fig. 1). The models shown in Figs. 6a and 6b are created based on the structures obtained after the hybrid MC/MD swapping procedure, replicated three times along the z-axis.

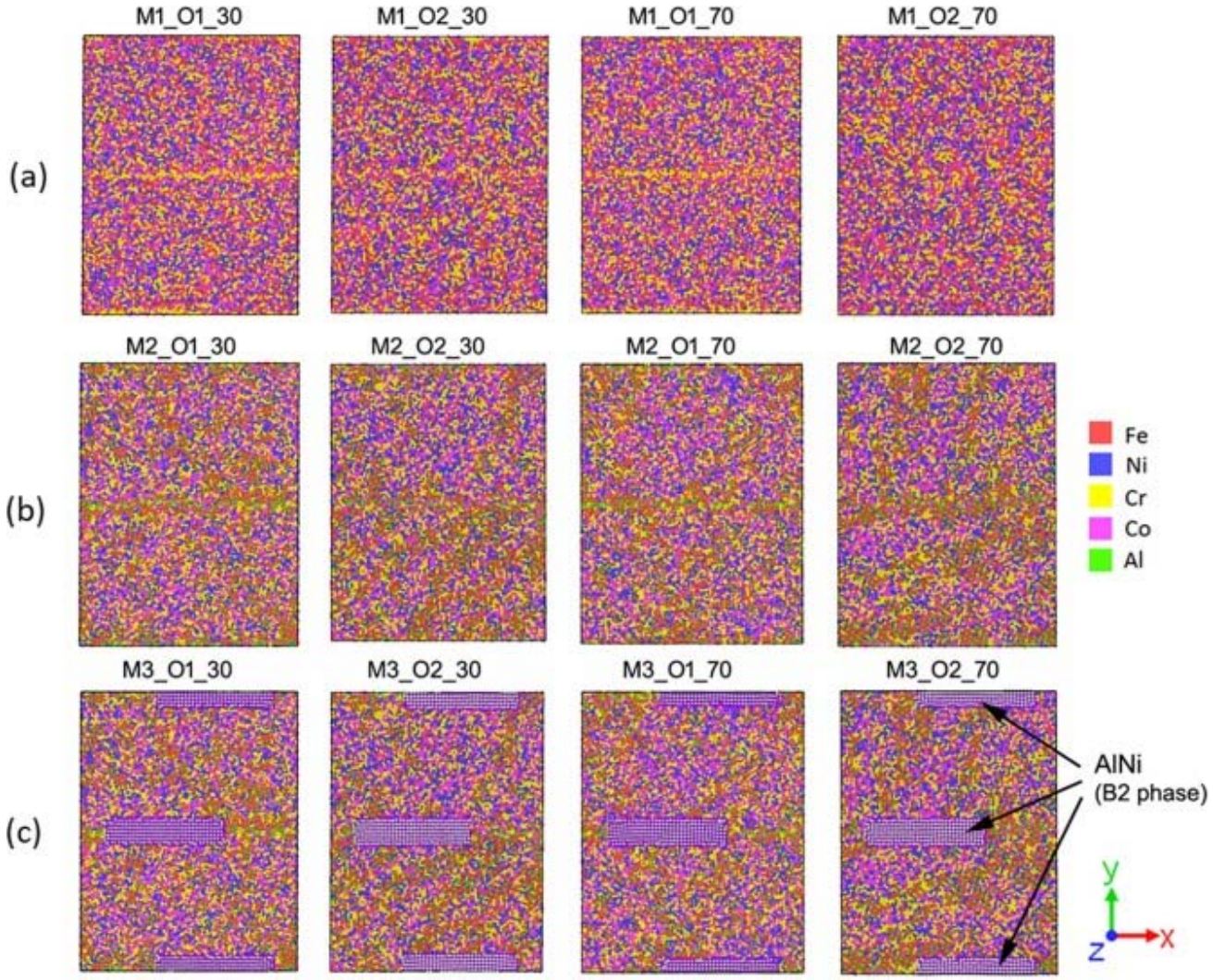

1. Download: Download high-res image (2MB)
2. Download: Download full-size image

Fig. 6. The 12 MD models used for the simulation of shear deformation. The structures in the top row (a) do not include Al (M1), those in the middle row (b) include Al (M2), and those in the bottom row (c) correspond to the material with Al in the matrix and the AlNi B2 intermetallic particles in the GBs (M3). The bi-crystals O1 have the misorientation axis [0 0 1], while for O2 the misorientation axis is [11¯0]. The misorientation angle θ (30° or 70°) is indicated for each structure.

The models in Fig. 6c are created from the replicated M2 samples, but they include AlNi B2 particles with dimensions of 9.5 nm × 2.4 nm × 0.7 nm at GBs that have been manually introduced using LAMMPS. The calculated lattice constant of AlNi is 3.002 Å. It should be noted that MC swapping does not result in the formation of this phase as the considered interatomic potential overestimates the heat of mixing for Al–Ni combination [24]. The crystallographic orientation of the B2 particles is set as x = [100], y = [010], and z = [001]. According to the available experimental data, the B2 phases enriched with Al and Ni are often observed at interfaces, including GBs, of HEAs

with a higher Al content. Therefore, the effect of such AlNi compounds on the shear deformation behaviour is of interest.

3.2.2. Shear deformation stress–strain curves

Fig. 7 shows the stress–strain curves plotted for the considered models subject to shear loading at 300 K in the *xy*-plane with a γ_{xy} value up to 0.5. In addition, the stress–strain relation for the materials M1 and M2 without MC swapping, i.e., without short-range ordering, is considered for comparison. Such materials having atoms randomly distributed within the samples are denoted as M1r and M2r, respectively. It should be noted that relatively strong oscillations are observed compared to those in common stress–strain curves of polycrystalline samples due to the high sensitivity of small bi-crystalline models to any deformation processes in the structure. However, the enhanced sensitivity facilitates the analyses of deformation mechanisms in the materials and helps to uncover the effect of different crystallographic orientations and GBs [29]. As the strain increases, the deformation of all the samples first occurs in the elastic deformation stage. Once the materials reach the yield point, the plastic flow region, i.e., the stage when plastic deformation appears, is initiated. The regions before and after this point are characterised by rapid strengthening and the decrease in stresses caused by the material relaxation, respectively. When the alloys with Al addition are subjected to further deformation, the stresses do not undergo significant changes but are maintained at a relatively stable value known as the flow stress. In the case of M1, the plastic deformation is characterised by stronger stress oscillations than those of the other two materials. This is especially evident for O2_30 and O2_70, for which GB segregation is suppressed (Fig. 3).

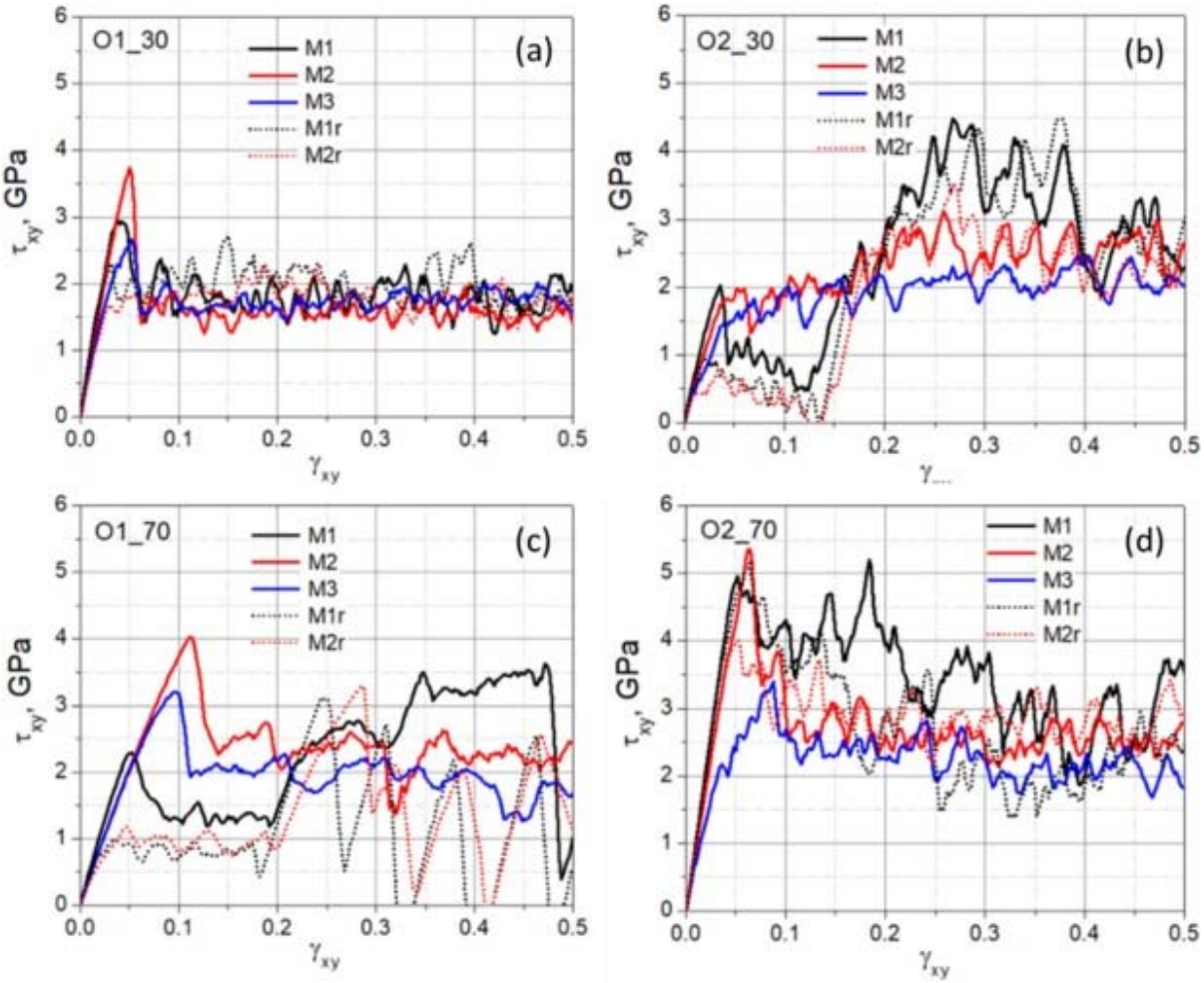

1. Download: Download high-res image (512KB)
2. Download: Download full-size image

Fig. 7. Shear deformation stress–strain curves for bi-crystals O1_30 (a), O2_30 (b), O1_70 (c), and O2_70 (d).

Table 1 shows the shear deformation yield strength τ_o, the stress value at the yield point, and the corresponding strain values γ_o for the considered structures. Overall, for three of the four different bi-crystal configurations, namely O1_30 (a), O1_70 (c), and O2_70 (d), M2 exhibits the highest yield strength among the three alloys, while for O2_30 (b), M1 demonstrates a slightly higher yield strength than M2. Only for the bi-crystal O1_70 (c), the yield strength of M3 is higher than that of M1. In all the other situations, the models with B2 inclusions at GBs demonstrate the lowest τ_o, indicating that such compounds in the GBs reduce the material strength.

Table 1. Shear deformation yield strength and strain for the considered models.

Material	O1_30		O2_30		O1_70		O2_70	
	τ_0, GPa	γ_0	τ_0, GPa	γ_0	τ_0, GPa	γ_0	τ_0, GPa	γ_0
M1	2.753	0.034	1.961	0.034	2.267	0.048	4.827	0.048
M2	3.739	0.050	1.805	0.040	3.953	0.108	5.349	0.062
M3	2.236	0.036	0.957	0.026	2.839	0.076	2.132	0.034

Overall, it can be seen from the comparison of the corresponding curves for the materials M1 (M2) and M1r (M2r) that the short-range ordering and GB segregation lead to an increase in shear deformation yield strength. The difference is less obvious for the case when the MC swapping does not result in the GB segregation formation, namely for M1_O2_70 (Fig. 3, Fig. 7).

3.2.3. Evolution of microstructure during shear deformation

Fig. 8 represents the microstructural evolution during the shear deformation for O1_30 and O1_70. To differentiate the lattice structures, the atoms are coloured by the common neighbour analysis (CNA) method according to their structure type. The green, blue, and red atoms have neighbours as in fcc, bcc, and hexagonal close-packed (hcp) lattices, respectively. The grey atoms do not belong to any of these structures and are located near lattice defects or amorphous regions. A vertical strip of tagged atoms, coloured in violet, is introduced to visualize the deformation mechanisms. The actual simulation cell is highlighted by a black frame, while an additional portion of the structure is attached at the top of each cell through a cell replication procedure in the y-direction to show the second GB.

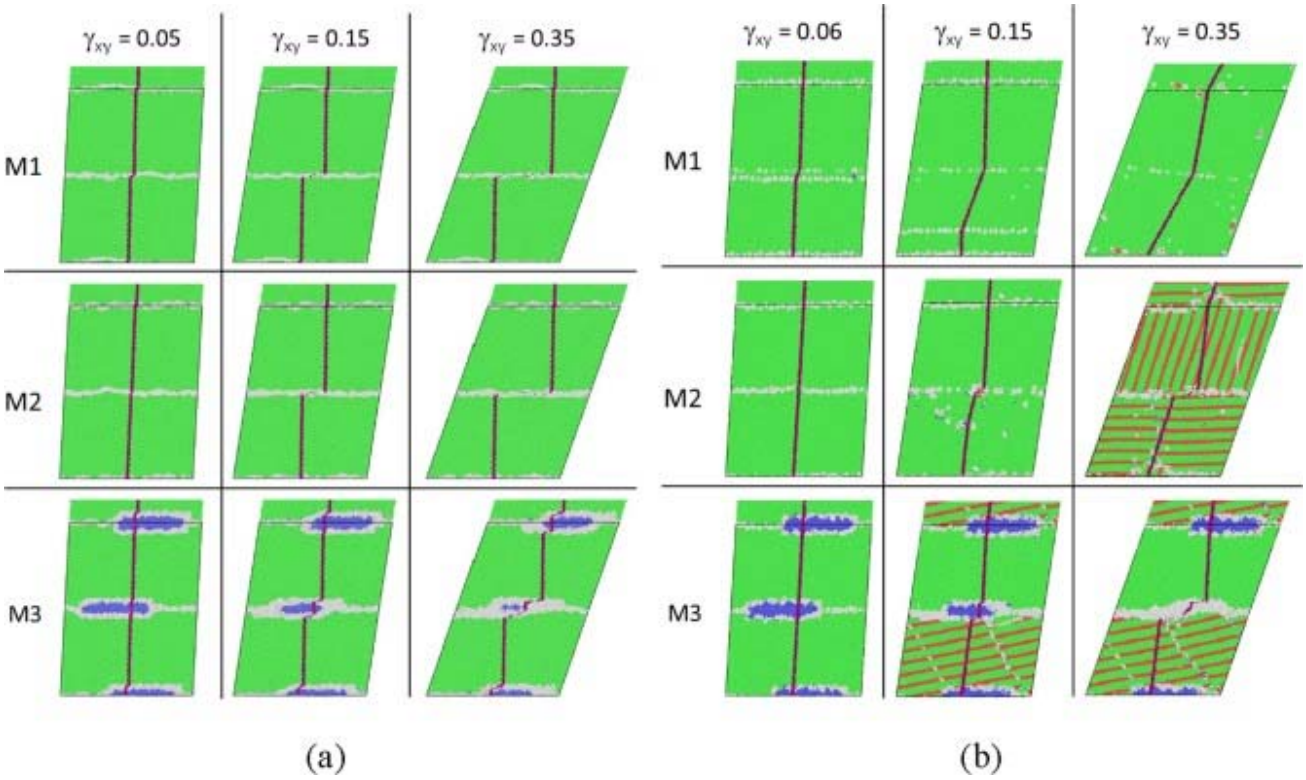

1. Download: Download high-res image (642KB)
2. Download: Download full-size image

Fig. 8. Microstructural evolution during shear deformation for O1_30 (a) and O1_70 (b). The atoms are coloured according to the CNA, where the fcc, hcp, and bcc/B2 structures are coloured in green, red, and blue, respectively, while the disordered structure at lattice defects is shown in light grey. (For interpretation of the references to colour in this figure legend, the reader can refer to the web version of this article.)

During the deformation of the bi-crystals O1_30 (Fig. 8a), the strips of tagged atoms remain vertical but with a break at the middle GB, indicating that the shear deformation is associated with active GB sliding. The fcc structure of the grains is preserved (the green colour) during the deformation process, indicating the absence of lattice defects, including stacking faults, inside the grains. For the material M1 with Cr atoms at GBs (Fig. 3a), grain boundary sliding starts slightly earlier (γ_o = 0.034) than that for M2 with GB segregation of Al (γ_o = 0.05) (Fig. 4a). As mentioned earlier, the critical stress τ_o required for the plastic flow caused by the GB sliding is higher for M2 (Table 1). Unlike the M1 and M2, for which the GB sliding occurs only along the central GB, the sliding is observed in both GBs of the cell for M3. Partial amorphization of the B2 inclusions, which starts at the B2/fcc interface area, facilitates the plastic deformation process.

Regarding the structural evolution in O1 bi-crystals with a larger misorientation angle θ of 70° (Fig. 8b), the plastic shear deformation of M1 starts with perpendicular migration of the central GB towards the opposite GB, accompanied by the gradual change in the inclination angle of the tagged atoms in the lower grain. This GB migration is associated with the motion of 1/2 ⟨1 1 0⟩ perfect dislocations from one GB to the opposite and their further transformation to leading and trailing 1/6 ⟨1 1 2⟩ Shockley

partial dislocations when a single-crystalline sample is finally formed. For comparison, the dislocation structures of the bi-crystals for M1 and M2 at γ_{xy} = 0.1 are shown in Fig. 9.

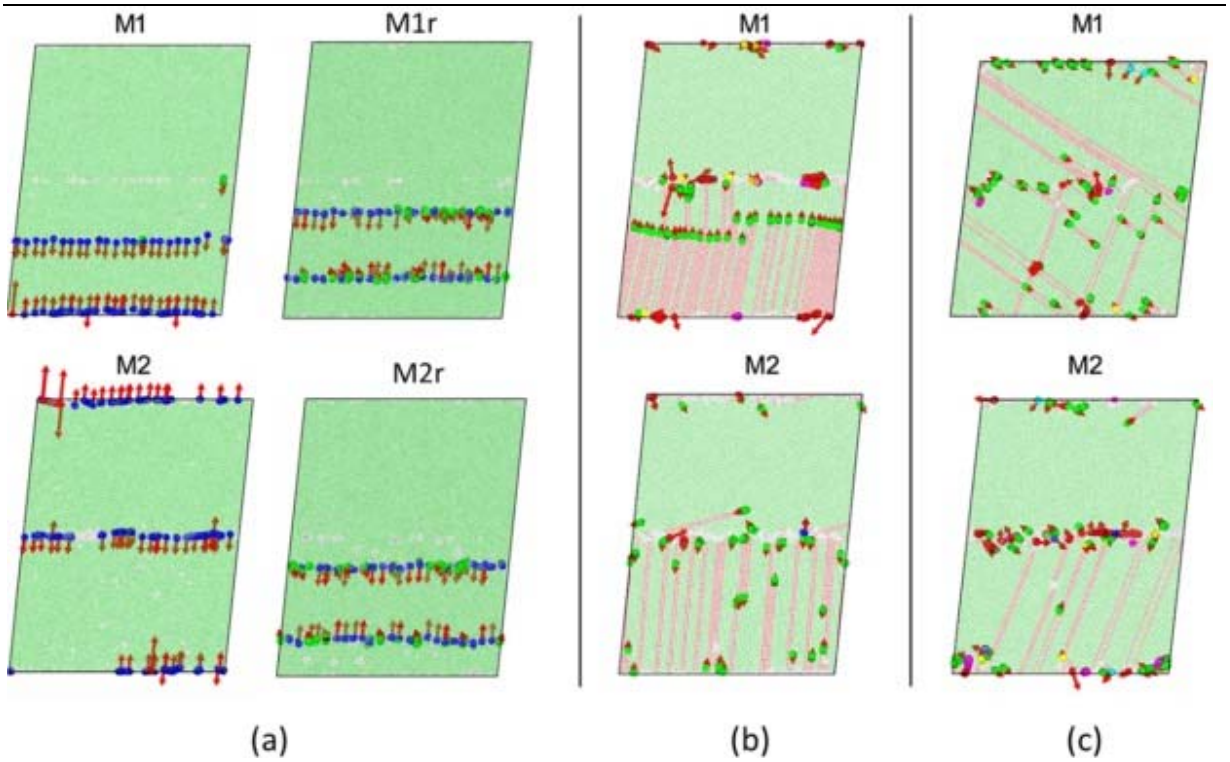

1. Download: Download high-res image (630KB)
2. Download: Download full-size image

Fig. 9. Dislocation structure of the bi-crystals O1_70 (a), O2_30 (b), and O2_70 (c) at γ_{xy} = 0.1. The corresponding material is denoted on the top of each snapshot. The dark blue, green, yellow, magenta, and light blue colours indicate the 1/2 ⟨1 1 0⟩ perfect dislocations, 1/6 ⟨1 1 2⟩ Shockley partial dislocations, 1/3 ⟨1 0 0⟩ Hirth dislocations, 1/6 ⟨1 1 0⟩ stair-rod dislocations, and 1/3 ⟨1 1 1⟩ Frank dislocations, respectively, while the red arrows demonstrate their Burgers vectors. (For interpretation of the references to colour in this figure legend, the reader can refer to the web version of this article.)

When γ_{xy} is below 0.2, such dislocation activity results in low critical stress to initiate the plastic flow in M1 as compared to that in the other two materials (Fig. 7c and Table 1). Further deformation of this material, approximately from γ_{xy} = 0.2, is associated with the material strengthening until the first intrinsic stacking fault (ISF) nucleates at γ_{xy} = 0.48, resulting in an abrupt decrease in the stress (Fig. 6c). Contrary to that in M1, the movement of perfect dislocations in the bi-crystals containing Al, i.e., M2, is suppressed (Fig. 9a), and GB migration is not observed. Up to γ_{xy} = 0.12, immobile sessile dislocations such as 1/3 ⟨1 0 0⟩ Hirth dislocations are formed by intersecting 1/6 ⟨1 1 2⟩ Shockley partial dislocations, which was also reported in [44]. Due to the absence of the GB migration mechanism at an early stage, the shear deformation yield strength of the materials with Al addition, especially M2, is much higher than that of M1. After that,

plastic deformation occurs because of the formation and propagation of mobile 1/6 ⟨1 1 2⟩ Shockley partial dislocations, leaving behind ISFs, as well as the GB sliding at higher strain levels (Fig. 8b). The B2 phase in GBs promotes the GB sliding, initiating the plastic flow early for M3, as compared with M2, leading to the absence of stacking faults in the upper crystal. Note that in the case of M1r and M2r, with randomly distributed atoms (without MC swapping), both the GBs move towards each other and meet in the middle of the lower grain regardless of the composition, leaving some lattice defects (Fig. 9a). Such lattice defects become nucleation sites for ISFs inside the grains. This is the reason for the abrupt decrease in stress at γ_{xy} = 0.25 and γ_{xy} = 0.27 in the M1r and M2r, respectively, followed by their strengthening and repeated relaxation when extrinsic stacking faults (ESFs) form (Fig. 7c). At the same time, in the M1 and M2, the formation of stacking faults is suppressed by the GB segregation.

Regarding the structures with the O2 orientation (Fig. 10), the crystallographic orientation of the lower grain in O2_30 bi-crystals promotes the nucleation of 1/6 ⟨1 1 2⟩ Shockley partial dislocations from the lower GB and their propagation towards the central GB (Fig. 9b), leaving behind a high density of ISF. The emergence of ISFs in M1 starts slightly earlier than that in M2, which contains Al atoms (Fig. 10a). The densities of leading Shockley partial dislocations and stacking faults in the lower grain of the materials with Al are not as high as those of M1, and the emission of stacking fault starts from both GBs simultaneously. As the strain increases, the high dislocation activity results in the formation of ISF in the upper crystal. It should be noted that for M1, further deformation results in the growth of the upper grain at the expense of the lower one. Such phenomenon can hardly be seen in the materials with Al addition. The GB sliding cannot be observed for M1 and M2. Similar to the previous case (O1_70), the plastic flow of M3 is realized through both the formation of ISF and GB sliding (Fig. 10a), meaning that the amorphization of the fcc/B2 interface facilitates the sliding process.

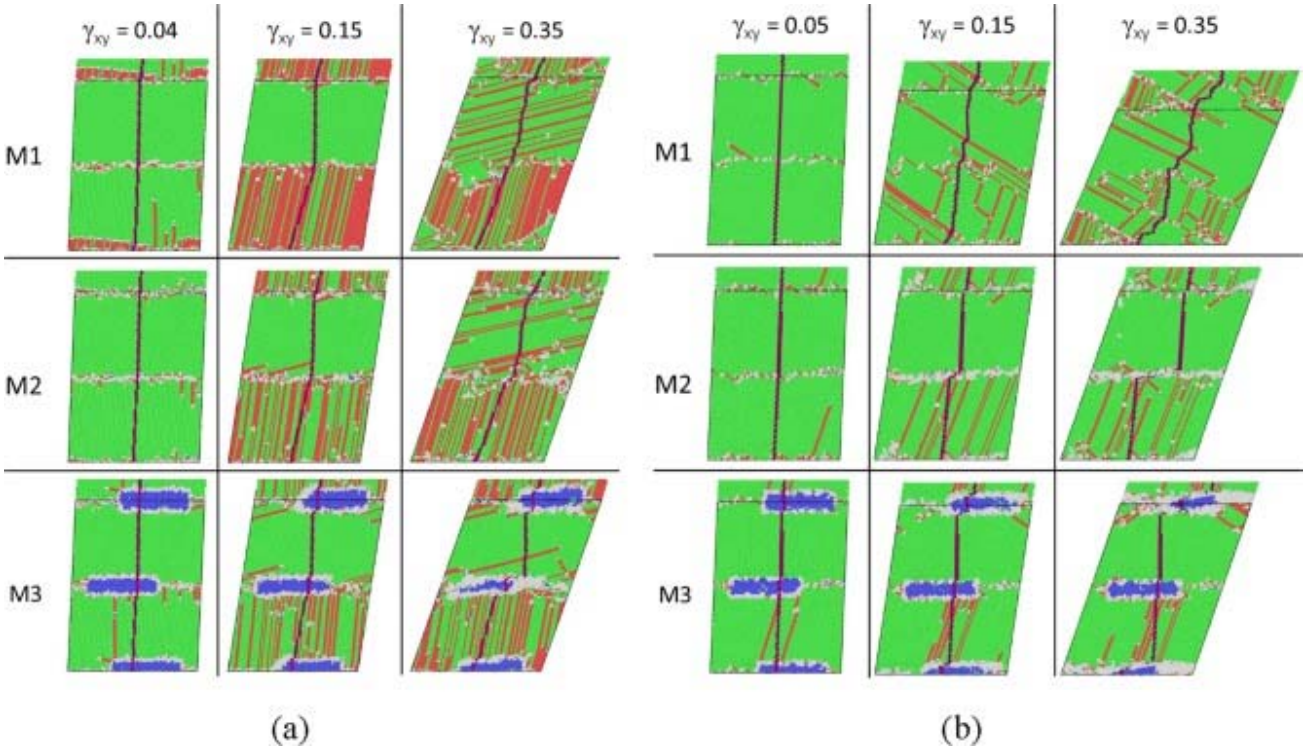

1. Download: Download high-res image (793KB)
2. Download: Download full-size image

Fig. 10. Microstructural evolution during shear deformation of O2_30 (a) and O2_70 (b). The atoms are coloured according to the CNA, where the fcc, hcp, and bcc/B2 structures are coloured in green, red, and blue, respectively, while the disordered structure at lattice defects is shown in light grey. (For interpretation of the references to colour in this figure legend, the reader can refer to the web version of this article.)

As for the bi-crystals O2_70 (Fig. 10b), unlike that in the other two materials, namely M2 and M3, the GB sliding in the M1 sample with no GB segregation (Fig. 3) and without Al atoms is suppressed. Its structure is characterised by unstable GBs and high densities of ISFs, ESFs, and deformation twins. Under deformation, continuous interaction between the defects (Fig. 9c) results in the orientation of the lower crystal gradually changing to the orientation of the upper crystal. After the deformation, only a small domain with initial orientation remains in the bi-crystal, which is similar to the deformation behaviour observed for the M1_O2_30 bi-crystal (Fig. 10a). The shape of the bi-crystal in M1 during shear deformation undergoes significant compression in the y-direction though there is no compressive stress applied in the y-direction. The addition of Al results in active GB sliding along one of the two GBs and a lower density of ISFs and ESFs. The latter happens slightly earlier in the sample with B2 inclusions. Stacking faults emerge at the B2/matrix interface, while their density is almost constant under further deformation due to the active GB sliding process.

4. Discussion

One of the driving forces for GB segregation is the relaxation of elastic strain energy created by solute atoms with a radius greater than that of the matrix. Solute atoms with a larger size than the average value of the matrix atoms in HEAs create compressive elastic strain in the material. When such solute atoms move to the GB, which have some free volume, the structure becomes more relaxed. Consequently, the atoms with the largest radius will tend to segregate to GBs. In Table 2, the atomic radii of the five constituent elements, taken from [45] are listed for comparison. The sizes of Al and Cr atoms, especially Al, are larger than those of the other constituent elements. The larger size indicates that the HEA with Al addition will have significant lattice distortion. The lattice distortion stimulates Al atoms to actively segregate to the GBs for HEAs with Al addition, while in the HEAs without Al, segregation of the second largest element, namely Cr, will occur. The Fe atoms, which has the third-largest radius, tend to form segregation after Al and Cr, resulting in the composition profile with bimodal distribution around the GB area (Fig. 3, Fig. 4).

Table 2. Atomic radii of the constituent elements.

Element	Fe	Ni	Cr	Co	Al
Atomic radius, nm	0.226	0.219	0.233	0.222	0.239

The second most important parameter for determining the ability of an element to form clusters and segregation is the mixing enthalpy. The driving force for short-range ordering and co-segregation, where two or more elements tend to be close to each other, is dictated by the tendency of such elements to mix [46], and therefore it is associated with the difference in the mixing enthalpy among the constituent elements. According to [24], all the binary random alloys consisting of element combinations excluding Al have relatively small heat of mixing, while the combinations including Al are characterised by much larger heat of mixing, which can be explained by the larger size of the Al atom. It is important to note that, unlike Al–Co, Al–Ni, and Al–Cr bonds for which the mixing enthalpy is positive, the combination of Al–Fe has a negative mixing enthalpy value (−4.824 kJ/mol) [24]. This provides a good explanation for both the strong tendency for the short-range ordering of Al and Fe atoms and the deficiency in the Co, Cr, and Ni content around the GBs enriched with Al and the formed Al–Fe clusters (Fig. 4).

Fig. 11 represents the radial distribution function (RDF) profiles of the models M1_O1_30 and M2_O1_30 after the hybrid MC/MD simulation for regions within grains and at the GB areas. Peaks in the RDF profiles, $g(r)$, correspond to the interatomic bond lengths, and therefore can provide information regarding the atomic structure of the studied HEAs and help to analyse the short-range ordering during the material equilibration via the MC swapping.

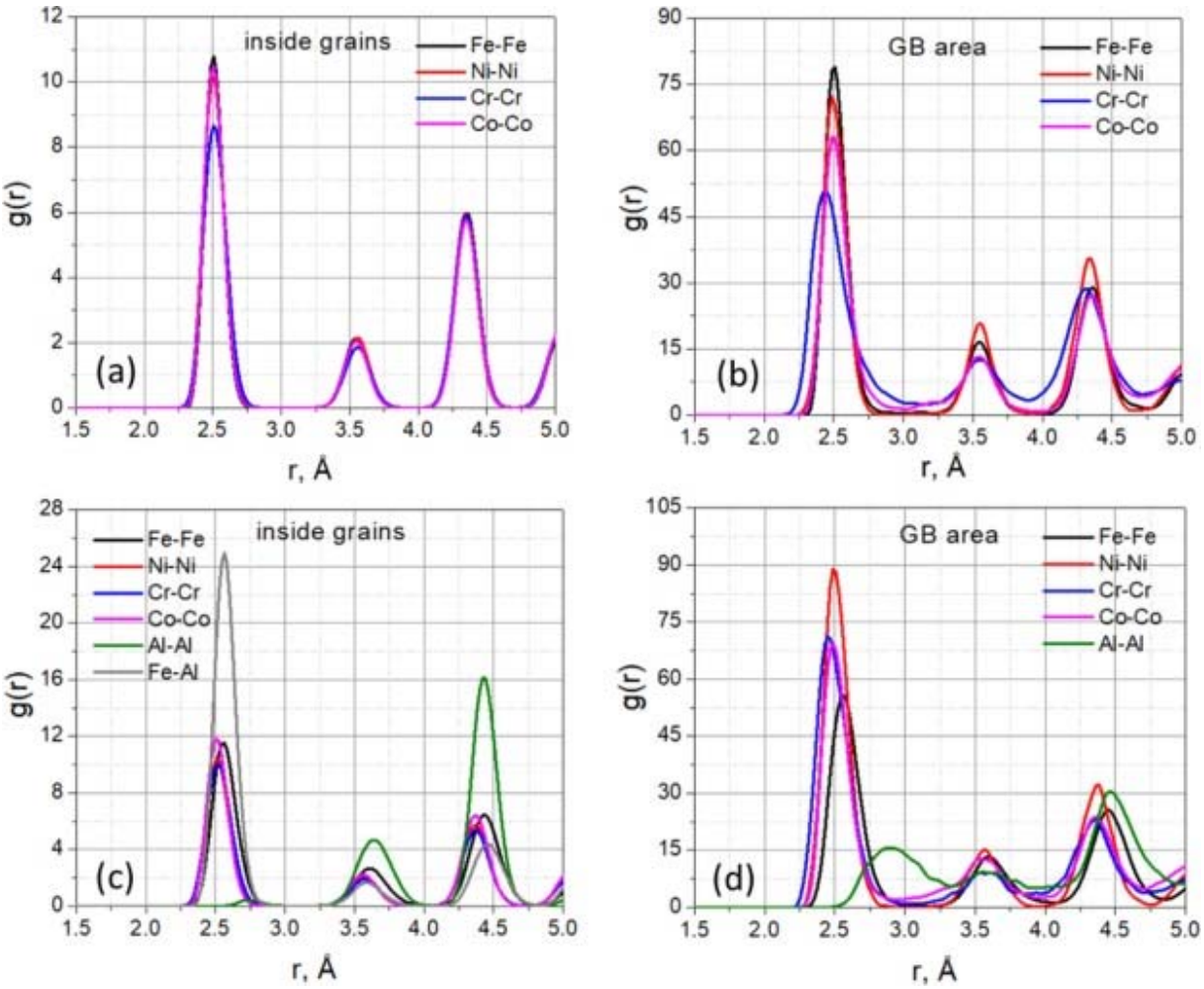

1. Download: Download high-res image (484KB)
2. Download: Download full-size image

Fig. 11. RDF profiles of M1_O1_30 (a, b) and M2_O1_30 (c, d) plotted for atoms inside the grains (a, c) and at the GB regions (b, d).

For the alloy without Al, within the grains (Fig. 11a) the RDF curves of Fe–Fe, Ni–Ni, Cr–Cr, and Co–Co bonds almost overlap each other and slightly differ only in the intensity of the first peaks ($r \approx 2.5$ Å). The overlapping is due to an equal contribution from all the element types due to their close size and the absence of significant lattice distortion in the fcc structure. However, in the GB areas (Fig. 11b), where strong segregation of Cr is observed for the bi-crystal O1_30 (Fig. 3), the RDF profile of Cr becomes broader and the first Cr–Cr peak shifts slightly to the left, indicating a more disordered structure and a more compact arrangement of the Cr atoms in such regions, respectively.

For the RDF curve of the Al–Al bonds inside the grains (Fig. 11c), the second and especially the third peak have a relatively high intensity due to short-range ordering, while the first peak has a low intensity. Such phenomenon can be explained by the strong contribution of the third Al–Al peak to the formation of ordered Al–Fe structure. In such a structure, the distance between Al atoms corresponds mostly to the third peak position. In contrast, in the GB area (Fig. 11d), the intensity of the first peak increases, while the

second and third ones have similar intensity. Similar to the RDF curve plotted for the Cr–Cr bonds in the GB areas, the peaks of the Al–Al bonds are broader, indicating a disordered distribution of the atoms. As compared to the material without Al, the presence of Al causes the peaks of the Fe–Fe bonds to shift to the right due to the tendency for local ordering of Fe with large Al atoms. The noticeable higher density of such clusters at the GB areas in the O2 bi-crystals than that in the O1 (Fig. 4) can be attributed to the difference in the crystallographic orientation, and consequently, to the difference in the GB free volume. The difference in the GB free volume for the considered bi-crystals can roughly be assessed through the number density computed for the computational cells. The calculated values for the bi-crystals O1_30, O1_70, O2_30, and O2_70 after their relaxation are 0.088754 $Å^{-3}$, 0.088726 $Å^{-3}$, 0.088788 $Å^{-3}$, and 0.088887 $Å^{-3}$, respectively. The density of O2_70 is the highest, indicating the lowest GB free volume for this case. On the contrary, for O1_70, the GB free volume is the highest. The relatively low free volume of the GBs after energy minimization in O2 bi-crystals leads to reduced elemental GB segregation as well as material M2r equilibration through intense Al–Fe ordering (Fig. 3, Fig. 4).

An important feature determining the deformation behaviour and the ability of an element to segregate is the GB stability. The GB stability is generally reflected by the GB energy, which in the case of a bi-crystal can be calculated by

$$GBE = \left(E_{gb} - NE_{0/at}\right)/(2A_{gb}), \quad (3)$$

where E_{gb} and $E_{o/at}$ are the energy of bi-crystals with and without GBs, respectively, N is the number of atoms in the bi-crystal, and A_{gb} is the GB area [47], [48]. The integer 2 corresponds to the number of GBs in the model. In general, GB segregation reduces the GB energy, and thus enhances the GB stability [49]. The calculated GB energy for the considered models before and after the MC swapping procedure are listed in Table 3. It is seen that the short-range ordering and the GB segregation reduces the energy of GBs, leading to their stabilization. After the MC swapping, the GB energy values of bi-crystals having GB segregation of Al are much lower than those of bi-crystals with GB segregation of Cr. The absence of GB segregation in M1_O2_70 (Fig. 3) can be attributed to the initial low-energy configuration of the bi-crystal (Fig. 2a) and thus the low GB energy and reduced free volume of the GBs. Indeed, it was shown earlier that GBs with higher interfacial energy and lower atomic densities (higher disorder and free volume) demonstrate better ability to segregate [46]. The significant reduction of the GB energy for the samples O1_70 after the MC swapping, especially in the case of the HEA containing Al, can be attributed to the high free volume of the GBs. This induces the high tendency to form GB segregation and Fe_3Al clustering near the GBs (Fig. 4c) that can decrease the GB energy down to a negative value [50].

Table 3. GB energy, mJ/m^2, calculated for the samples with (M1 and M2) and without the MC swapping (M1r and M2r).

Empty Cell	**O1_30**	**O1_70**	**O2_30**	**O2_70**
M1r	1364.503	1416.295	1356.075	783.236
M1	1227.358	1026.835	1061.240	495.664

Empty Cell	**O1_30**	**O1_70**	**O2_30**	**O2_70**
M2r	732.707	1021.945	860.025	598.029
M2	476.455	–61.786	787.455	140.171

The ability to stabilize GBs by the formed GB segregation is also proved by the fact that plastic deformation starts earlier in the samples without such structural elements (see curves for M1r and M2r in Fig. 7). The critical stress required to initiate the plastic flow in such materials is lower.

It is believed that at a higher dopant concentration or a lower temperature, the resistance to GB migration is greater [51]. Even though the concentration of Al atoms in the GBs in M2_O1_70 is lower than that of Cr in M1_O1_70 (Fig. 3, Fig. 4), the shear-coupled GB migration can be observed in the latter case (Fig. 8, Fig. 9). This indicates that the resistance to GB migration is greater for Al atoms than Cr atoms. The GB migration of a material with solute atoms increases as their drag force decreases. The drag force is enhanced as the size mismatch between the matrix and solute atoms increases [52]. As mentioned earlier, the size of the Al atom is larger compared to that of the Cr atoms (Table 2). However, when the GB energy is large enough and consequently the activation energy for GB migration is small, the incorporation of solute atoms does not effectively impede the GB motion. The GB migration of the M1_O1_70 material with GB segregation of Cr can be attributed to the high GB energy. Even though the GB energy decreases after the material reaches an equilibrium, the formation of GB segregation of Cr is not sufficient for stabilizing the GB.

Along with the GB stabilizing effect, the absence of the shear-coupled GB migration in the other considered structures, including O1 with a lower misorientation angle (θ = 30°), can be associated with the crystallographic orientation effect. For instance, it has been found that the mobility of low-angle GBs is lower than that of high-angle GBs [53].

In the case of O2 (Fig. 10), regardless of the misorientation angle, it is revealed that in the presence of GB segregation, the propagation and interaction of dislocations and ISFs are impeded and confined within grains (Figs. 9b and 9c). When the GB segregation is suppressed, as observed for M1 (Fig. 3), the active dislocation interaction and formation of stacking faults and twins result in gradual relocation of the GBs. The relatively low density of stacking faults in the materials with ordered Fe_3Al clusters compared with that of M1 can also indicate the increased stacking fault energy in such materials. To verify this, the generalized stacking fault energy (GSFE) is calculated for the random HEAs and the Fe_3Al intermetallic compound.

It is believed that the most commonly occurring fcc-based structures among intermetallic compounds with a stoichiometric ratio of 3:1 are the cubic $L1_2$ and the tetragonal $D0_{22}$ structures (see Fig. 12a, panels for the RDF curves and corresponding lattices), which have subtle crystallographic differences [54], [55], [56], [57]. Note that the calculated lattice parameter a, is the same for both structures of Fe_3Al and found to be 3.734 Å in the current study. The calculated a is relatively close to that found in other works for the $L1_2$ (~3.47–3.67 Å [58], [59]) and to the fcc lattice parameter of the HEA with Al addition (~3.58 Å [24]). The formation of lamellar structures with ordered

$L1_2$ phases in the as-cast HEAs having Al addition was earlier reported in several experimental works [10], [60], [61], [62]. It is believed that the $L1_2$ structure in HEAs can be formed by Al and Fe, as well as Co, Cr, and Ni atoms [61]. However due to the low enthalpy of mixing for the Al–Fe pairs compared to that of the other elemental combinations, the ordered phase is formed mostly by the Al and Fe atoms. The RDF curves of the $D0_{22}$ structure are more similar to the RDF curves of HEA with Al addition than the curves of the $L1_2$ structure. The RDF curves of the former two materials show a high-intensity Al–Al peak at $r \approx 4.45$ Å (Fig. 11, Fig. 12), indicating that the ordering in the HEA with Al addition leads to the formation Fe_3Al clusters with the $D0_{22}$ structure.

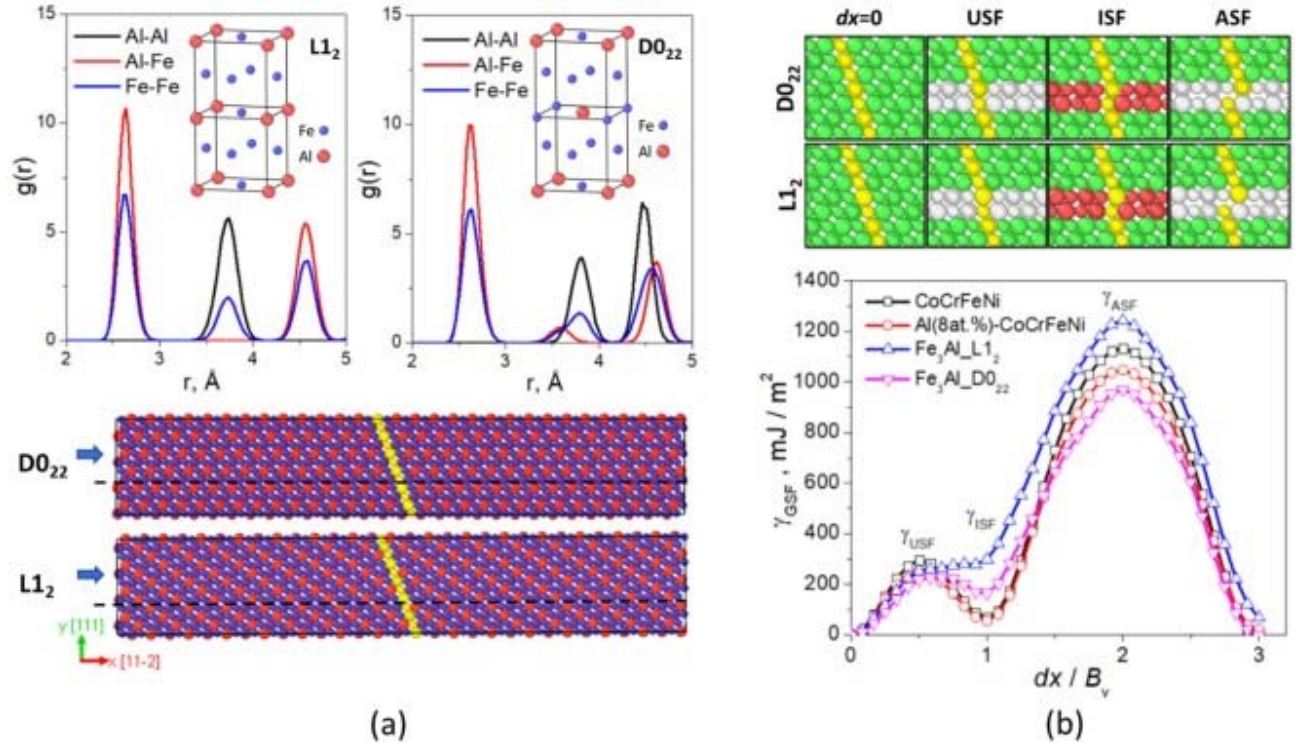

1. Download: Download high-res image (575KB)
2. Download: Download full-size image

Fig. 12. (a) RDFs with corresponding lattices (the top panels) and initial atomic structures of $L1_2$- and $D0_{22}$-type Fe_3Al used for the GSFE calculation (the bottom panel). The Al and Fe atoms are shown in red and blue, respectively. The yellow line is introduced to make the atom displacement more visible. (b) CNA for the initial and defected $L1_2$- and $D0_{22}$-type Fe_3Al obtained during the displacement of atomic layers along the $[11\bar{2}]$ direction (the top panel). To differentiate the atom types, the Al atoms are represented in a bigger size. USF, ISF, and ASF denote unstable, intrinsic, and aligned stacking faults, respectively. The dependence of GSFE γ_{GSF} for the Fe_3Al structures and the random CoCrFeNi and Al (8 at%)-CoCrFeNi HEAs on the displacement dx normalized over the corresponding Burgers vector (Bv) of a Shockley partial dislocation (the bottom panel). (For interpretation of the references to colour in this figure legend, the reader can refer to the web version of this article.)

For calculating the GSFE, the simulation approach described in several recent works [44], [63], [64] is applied. Four different materials, namely the CoCrFeNi and Al (8 at%)-CoCrFeNi HEAs with atoms randomly distributed within materials (i.e., without MC swapping procedure) and the Fe_3Al intermetallic compounds having the $L1_2$ and $D0_{22}$ structures are considered. In Fig. 12a, the models for the GSFE calculation are presented only for the intermetallic compounds $L1_2$ and $D0_{22}$. To introduce stacking faults into the simulation cell, the atoms below the dashed black horizontal line are fixed, while the remaining atoms are being shifted in the $[11\bar{2}]$ direction.

As can be seen from the Fig. 12b, the GSFE curve for each material has two maxima, which are associated with the formation of the so-called unstable and aligned stacking faults, and the minimum between them is associated with the formation of an ISF. These defect structures are characterised by the corresponding energy denoted as γ_{USF}, γ_{ISF}, and γ_{ASF}, respectively. The stacking fault energy is normally assessed based on the γ_{ISF}. It is clearly seen that the stacking fault energy for the intermetallic compounds, especially for the Fe_3Al with the $L1_2$ structure, is higher than that for the random HEAs. For the HEAs with and without Al, the γ_{ISF} values are 55.94 mJ/m^2 and 69.26 mJ/m^2, respectively, while for $D0_{22}$- and $L1_2$-type Fe_3Al, the values are 164.93 mJ/m^2 and 298.74 mJ/m^2, respectively. Note that the calculated stacking fault energy values for the random HEA are in quantitative agreement with the values obtained in [24]. Such high energy for the ordered intermetallic compounds, especially those having the $L1_2$ structure, is due to the formation of an energetically unfavourable atomic configuration, where the large Al atoms in the faulted plane are brought in close contact with other Al atoms (Fig. 12b). In the random HEAs with Al, such Al–Al bonds might already exist in the unfaulted sample. In addition, the probability for one Al atom to meet another during the displacement of the atomic planes is smaller than that in the intermetallic compounds, and the introduced stacking fault does not result in an excess formation of such bonds, thus explaining the reduced ISF energy. The obtained γ_{ISF} values for Fe_3Al and HEAs without MC swapping indicate that the local ordering increases the stacking fault energy of the HEA. The increased stacking fault energy of the Fe_3Al phase found in the study agrees with a recent study reporting that the short-range ordering increases the stress required to nucleate the Shockley partial dislocation [65].

In general, the results of shear deformation modeling demonstrate that the shear deformation yield strength of the material M2 with elemental segregation of Al/Fe at the GBs and the Al–Fe clusters is higher than that of material M1 with segregation of Cr/Fe at the GBs and especially that of M3 with B2 inclusions (Table 1). The improved strength of the HEA with Al addition agrees with the previous experimental studies [9]. However, the material M3 with B2 particles at the GBs demonstrates reduced shear strength. Thanks to the GB stabilization effect, the formed elemental GB segregation of both Al and Cr resists the GB sliding and leads to the increased shear deformation yield strength. Due to bond breakage and grinding of the B2/fcc interface, this deformation mechanism becomes more favourable in the sample with the AlNi intermetallic particles inclusion, leading to the decreased yield strength. In the latter case, the reduced strength of the HEAs with B2 inclusions observed in the current work can be attributed to the small computational cell size and consequently small B2 particles. For example, after the laser powder bed fusion, the B2 particles have a diameter of at least hundreds of nanometers [9], which is difficult to realize in the MD study due to the limited spatial

scale. However, understanding the effect of such intermetallic compounds at GBs, similar to the considered models, on the deformation mechanisms could help to predict and analyse the deformation behaviour of nano-grained HEAs with GB segregation of AlNi.

5. Summary

In this work, the short-range ordering and GB segregation were studied for equiatomic CoCrFeNi and quinary Al (8 at%)-CoCrFeNi HEAs in four different bi-crystalline models using the hybrid MC/MD simulation. The effects of such an equilibration process and the presence of AlNi intermetallic compounds with B2 lattice structure at GBs on the shear deformation behaviour of the bi-crystals at 300 K were further investigated utilizing the MD modeling. The major conclusions are drawn as follows.

The equilibration process and local ordering via the MC/MD simulation lead to the segregation of Cr and Fe to GBs in the material without Al addition. In the alloy with Al addition, this procedure results in segregation of Al and Fe to GBs and the formation of Fe_3Al intermetallic compounds with the $D0_{22}$ structure.

The formation of Fe_3Al clusters and elemental co-segregation to GBs is dictated by the lattice distortion caused by the atomic size difference of the constituent elements as well as their heat of mixing. Another important factor is the crystallographic orientation. Thus, the segregation of Cr to the GBs of O2 bi-crystals, especially with $\theta = 70°$, is suppressed due to the initially low-energy configuration and lower GB free volume than those of O1. The large Al atoms in M2 create significant lattice distortion and lead to high energy for the material. Therefore, the GB segregation of Al can be observed for all the considered cases. However, for O2, the ability of Al to segregate is slightly reduced, and the energy minimization occurs mostly through the formation of Fe_3Al clusters.

It is revealed that the Fe_3Al compounds have increased stacking fault energy compared to those for the considered HEAs without short-range ordering. The stress required to nucleate the Shockley partial dislocations in HEAs with such compounds is higher, which results in the enhanced strength of the material.

In the absence of the GB segregation, the GBs are not stable. As a result of active lattice defect interaction, the GBs gradually relocate during the shear deformation, and one of the grains gradually grows at the expense of another. Overall, the ability to stabilize GBs is higher for Al than that for Cr. Thus, unlike the case of M1_O1_70, the GB migration is not observed in the corresponding bi-crystals with Al present at the GB region, resulting in the increased shear deformation yield strength.

Caused by the GB stabilization effect, the GB segregation suppresses GB motion and resists the GB sliding. At the same time, the AlNi intermetallic particles with the B2 structure located at the GBs of bi-crystals M3 facilitate the plastic deformation process through the active GB sliding due to their partial amorphization starting from the B2/fcc interface area, which leads to the reduced shear deformation yield strength in comparison with that of the other materials, namely M1 and M2.

CRediT authorship contribution statement

Rita Babicheva: Conceptualization, Methodology, Software, Data curation, Visualization, Formal analysis, Writing – original draft. **Asker Jarlöv:** Methodology, Software, Formal analysis, Visualization, Writing – review & editing. **Han Zheng:** Writing – review & editing. **Sergey Dmitriev:** Methodology, Writing – review

& editing. **Elena Korznikova:** Writing – review & editing. **Mui Ling Sharon Nai:** Supervision, Writing – review & editing. **Upadrasta Ramamurty:** Conceptualization, Validation, Resources, Funding acquisition, Project administration, Supervision, Writing – review & editing. **Kun Zhou:** Conceptualization, Validation, Resources, Funding acquisition, Supervision, Writing – review & editing.

Declaration of Competing Interest

The authors declare that they have no known competing financial interests or personal relationships that could have appeared to influence the work reported in this paper.

Acknowledgements

This work is funded by the Structural Metals and Alloys Programme (Grant reference No. A18b1B0061) of the Agency for Science, Technology and Research (A*STAR) of Singapore. A. Jarlöv is grateful for the scholarship from the A*STAR Graduate Academy, Singapore. E. Korznikova acknowledges the financial support offered by the grant of the Russian Science Foundation (No. 21-12-00275). R. Babicheva gratefully thanks the high-performance computing resource offered by Nanyang Technological University, Singapore.

Data availability

The authors do not have permission to share data.

References

[1]

B. Cantor, I.T.H. Chang, P. Knight, A.J.B. Vincent

Microstructural development in equiatomic multicomponent alloys

Mater. Sci. Eng., A, 375 (2004), pp. 213-218, 10.1016/j.msea.2003.10.257
View PDFView articleView in ScopusGoogle Scholar
[2]

J.-W. Yeh, S.-K. Chen, S.-J. Lin, J.-Y. Gan, T.-S. Chin, T.-T. Shun, C.-H. Tsau, S.-Y. Chang

Nanostructured high-entropy alloys with multiple principal elements: novel alloy design concepts and outcomes

Adv. Eng. Mater., 6 (5) (2004), pp. 299-303, 10.1002/adem.200300567
Google Scholar
[3]

K.-Y. Tsai, M.-H. Tsai, J.-W. Yeh

Sluggish diffusion in Co–Cr–Fe–Mn–Ni high-entropy alloys

Acta Mater., 61 (13) (2013), pp. 4887-4897, 10.1016/j.actamat.2013.04.058
View PDFView articleView in ScopusGoogle Scholar
[4]

Z.M. Li, K.G. Pradeep, Y. Deng, D. Raabe, C.C. Tasan

Metastable high-entropy dual-phase alloys overcome the strength-ductility trade-off

Nature, 534 (7606) (2016), pp. 227-230, 10.1038/nature17981
View in ScopusGoogle Scholar
[5]

E.P. George, W. Curtin, C.C. Tasan

High entropy alloys: a focused review of mechanical properties and deformation mechanisms

Acta Mater., 188 (2020), pp. 435-474, 10.1016/j.actamat.2019.12.015
View PDFView articleView in ScopusGoogle Scholar

[6]

S.J. Zinkle, L.L. Snead

Designing radiation resistance in materials for fusion energy

Annu. Rev. Mater. Res., 44 (2014), pp. 241-267, 10.1146/annurev-matsci-070813-113627
View in ScopusGoogle Scholar
[7]

M.A. Hemphill, T. Yuan, G.Y. Wang, J.W. Yeh, C.W. Tsai, A. Chuang, P.K. Liaw

Fatigue behavior of Al0.5CoCrCuFeNi high entropy alloys

Acta Mater., 60 (2012), pp. 5723-5734, 10.1016/j.actamat.2012.06.046
View PDFView articleView in ScopusGoogle Scholar
[8]

M.-H. Chuang, M.H. Tsai, W.-R. Wang, S.-J. Lin, J.-W. Yeh

Microstructure and wear behavior of AlxCo1.5CrFeNi1.5Tiy high-entropy alloys

Acta Mater., 59 (16) (2011), pp. 6308-6317, 10.1016/j.actamat.2011.06.041
View PDFView articleView in ScopusGoogle Scholar
[9]

Sun Z., Tan X., Wang C., Descoins M., Mangelinck D., Tor S.B., Jägle E.A., Zaefferer S., Raabe D.. Reducing hot tearing by grain boundary segregation engineering in additive manufacturing: example of an AlxCoCrFeNi high-entropy alloy. Acta Materialia, 2021, **204**: 116505 (14 pages). 10.1016/j.actamat.2020.116505.
Google Scholar
[10]

Bhattacharjee T., Wani I. S., Sheikh S., Clark I.T., Okawa T., Guo S., Bhattacharjee P. P., Tsuji N.. Simultaneous Strength-Ductility Enhancement of a Nano-Lamellar AlCoCrFeNi2.1 Eutectic High Entropy Alloy by Cryo-Rolling and Annealing. Scientific Reports, 2018, **8**: 3276 (8 pages). 10.1038/s41598-018-21385-y.
Google Scholar
[11]

K. Jasiewicz, J. Cieslak, S. Kaprzyk, J. Tobola

Relative crystal stability of AlxFeNiCrCo high entropy alloys from XRD analysis and formation energy calculation

J. Alloy. Compd., 648 (2015), pp. 307-312, 10.1016/j.jallcom.2015.06.260
View PDFView articleView in ScopusGoogle Scholar
[12]

Y.-F. Kao, T.-J. Chen, S.-K. Chen, J.-W. Yeh

Microstructure and mechanical property of as-cast, -homogenized, and -deformed AlxCoCrFeNi (0 ≤x ≤2) high-entropy alloys

J. Alloy. Compd., 488 (1) (2009), pp. 57-64, 10.1016/j.jallcom.2009.08.090
View PDFView articleView in ScopusGoogle Scholar
[13]

T. Yang, S. Xia, S. Liu, C. Wang, S. Liu, Y. Zhang, J. Xue, S. Yan, Y. Wan g

Effects of Al addition on microstructure and mechanical properties of AlxCoCrFeNi high-entropy alloy

Mater. Sci. Eng., A, 648 (2015), pp. 15-22, 10.1016/j.msea.2015.09.034
View PDFView articleView in ScopusGoogle Scholar
[14]

D.B. Miracle, O.N. Senkov

A critical review of high entropy alloys and related concepts

Acta Mater., 122 (2017), pp. 448-511, 10.1016/j.actamat.2016.08.081
View PDFView articleView in ScopusGoogle Scholar
[15]

Hayun S., Lilova K., Salhov S., Navrotsky A.. Enthalpies of formation of high entropy and multicomponent alloys using oxide melt solution calorimetry. Intermetallics, 2020, **125**: 106897 (7 pages). 10.1016/j.intermet.2020.106897.
Google Scholar
[16]

C. Li, M. Zhao, J.C. Li, Q. Jiang

B2 structure of high-entropy alloys with addition of Al

J. Appl. Phys., 104 (2008), pp. 113504-113506, 10.1063/1.3032900
View in ScopusGoogle Scholar

[17]

Asghari-Rad P., Nguyen N.T.-C., Zargaran A., Sathiyamoorthi P., Kim H.S.. Deformation-induced grain boundary segregation mediated high-strain rate superplasticity in medium entropy alloy. Scripta Materialia, 2022, **207**: 114239 (5 pages). 10.1016/j.scriptamat.2021.114239.
Google Scholar
[18]

Ming K., Li L., Li Z., Bi X., Wang J.. Grain boundary decohesion by nanoclustering Ni and Cr separately in CrMnFeCoNi high-entropy alloys. Science Advances, 2019, **5**(12): eaay0639 (7 pages). 10.1126/sciadv.aay0.
Google Scholar
[19]

K. Cho, Y. Fujioka, T. Nagase, H.Y. Yasuda

Grain refinement of non-equiatomic Cr-rich CoCrFeMnNi high-entropy alloys through combination of cold rolling and precipitation of σ phase

Mater. Sci. Eng., A, 735 (2018), pp. 191-200, 10.1016/j.msea.2018.08.038
View PDFView articleView in ScopusGoogle Scholar
[20]

Heczko M., Mazánová V., Gröger R., Záležák T., Hooshmand M.S., George E.P., Mills M.J., Dlouhý A.. Elemental segregation to lattice defects in the CrMnFeCoNi high-entropy alloy during high temperature exposures. Acta Materialia, 2021, **208**: 116719 (15 pages). 10.1016/j.actamat.2021.116719.
Google Scholar
[21]

Zhao S.. Effects of local elemental ordering on defect-grain boundary interactions in high-entropy alloys. Journal of Alloys and Compounds, 2021, **887**: 161314 (15 pages). 10.1016/j.jallcom.2021.161314.
Google Scholar
[22]

D. Utt, A. Stukowski, K. Albe

Grain boundary structure and mobility in high-entropy alloys: a comparative molecular dynamics study on a Σ11 symmetrical tilt grain boundary in face-centered cubic CuNiCoFe

Acta Mater., 186 (2020), pp. 11-19, 10.1016/j.actamat.2019.12.031
View PDFView articleView in ScopusGoogle Scholar
[23]

Wynblatt P., Chatain D.. Modeling grain boundary and surface segregation in multicomponent high-entropy alloys. Physical Review Materials, 2019, **3**: 054004 (8 pages). 10.1103/PhysRevMaterials.3.054004.
Google Scholar
[24]

D. Farkas, A. Caro

Model interatomic potentials for Fe–Ni–Cr–Co–Al high-entropy alloys

J. Mater. Res., 35 (2020), pp. 3031-3040, 10.1557/jmr.2020.294
View in ScopusGoogle Scholar
[25]

M.M. Gong, F. Liu, Y.Z. Chen

Modeling solute segregation in grain boundaries of binary substitutional alloys: effect of excess volume

J. Alloy. Compd., 682 (2016), pp. 89-97, 10.1016/j.jallcom.2016.04.284
View PDFView articleView in ScopusGoogle Scholar
[26]

Tschopp M.A., Solanki K.N., Gao F., Sun X., Khaleel M.A., Horstemeyer M.F.. Probing grain boundary sink strength at the nanoscale: energetics and length scales of vacancy and interstitial absorption by grain boundaries in α-Fe. Physical Review B, 2012, **85**: 064108 (21 pages). 10.1103/PhysRevB.85.064108.
Google Scholar
[27]

R.I. Babicheva, S.V. Dmitriev, Y. Zhang, S.W. Kok, N. Srikanth, B. Liu, K. Zhou

Effect of grain boundary segregations of Fe Co, Cu, Ti, Mg and Pb on small plastic deformation of nanocrystalline Al

Comput. Mater. Sci., 98 (2015), pp. 410-416, 10.1016/j.commatsci.2014.11.038
View PDFView articleView in ScopusGoogle Scholar
[28]

R.I. Babicheva, D.V. Bachurin, S.V. Dmitriev, Y. Zhang, S.W. Kok, L. Bai, K. Zhou

Elastic moduli of nanocrystalline binary Al alloys with Fe Co, Ti, Mg and Pb alloying elements

Phil. Mag., 96 (15) (2016), pp. 1598-1612, 10.1080/14786435.2016.1171416
View in ScopusGoogle Scholar
[29]

R.I. Babicheva, S.V. Dmitriev, L. Bai, Y. Zhang, S.W. Kok, G. Kang, K. Zhou

Effect of grain boundary segregation on the deformation mechanisms and mechanical properties of nanocrystalline binary aluminium alloys

Comput. Mater. Sci., 117 (2016), pp. 445-454, 10.1016/j.commatsci.2016.02.013
View PDFView articleView in ScopusGoogle Scholar
[30]

R.I. Babicheva, S.V. Dmitriev, D.V. Bachurin, N. Srikanth, Y. Zhang, S.W. Kok, K. Zhou

Effect of grain boundary segregation of Co or Ti on cyclic deformation of aluminium bi-crystals

Int. J. Fatigue, 102 (2017), pp. 270-281, 10.1016/j.ijfatigue.2017.01.038
View PDFView articleView in ScopusGoogle Scholar
[31]

S. Plimpton

Fast Parallel Algorithms for Short-Range Molecular Dynamics

J. Comput. Phys., 117 (1995), pp. 1-19, 10.1006/jcph.1995.1039
View PDFView articleView in ScopusGoogle Scholar
[32]

D. Farkas, A. Caro

Model interatomic potentials and lattice strain in a high-entropy alloy

J. Mater. Res., 33 (19) (2018), pp. 3218-3225, 10.1557/jmr.2018.245
View in ScopusGoogle Scholar
[33]

Stukowski A.. Visualization and analysis of atomistic simulation data with OVITO–the Open Visualization Tool. Modelling and Simulation in Materials Science and Engineering, 2009, **18**(1): 015012 (8 pages). 10.1088/0965-0393/18/1/015012.
Google Scholar
[34]

J. Joseph, N. Stanford, P. Hodgson, D.M. Fabijanic

Understanding the mechanical behaviour and the large strength/ductility differences between FCC and BCC AlxCoCrFeNi high entropy alloys

J. Alloy. Compd., 726 (2017), pp. 885-895, 10.1016/j.jallcom.2017.08.067
View PDFView articleView in ScopusGoogle Scholar
[35]

Wei F., Wei S., Lau K.B., Teh W.H., Lee J.J., Seng H.L., Tan C.C., Wang P., Ramamurty U.. Compositionally graded AlxCoCrFeNi high-entropy alloy manufactured by laser powder bed fusion. Materialia, 2022, **21**, 101308 (10 pages). 10.1016/j.mtla.2021.101308.
Google Scholar
[36]

P. Hirel

Atomsk: A tool for manipulating and converting atomic data files

Comput. Phys. Commun., 197 (2015), pp. 212-219, 10.1016/j.cpc.2015.07.012
View PDFView articleView in ScopusGoogle Scholar
[37]

M.A. Tschopp, S.P. Coleman, D.L. McDowell

Symmetric and asymmetric tilt grain boundary structure and energy in Cu and Al (and transferability to other fcc metals)

Integrating Mater. Manuf. Innovation, 4 (2015), pp. 176-189, 10.1186/s40192-015-0040-1
View in ScopusGoogle Scholar
[38]

N. Metropolis, A.W. Rosenbluth, M.N. Rosenbluth, A.H. Teller, E. Teller

Equation of state calculations by fast computing machines

J. Chem. Phys., 21 (1953), pp. 1087-1092, 10.1063/1.1699114
View in ScopusGoogle Scholar
[39]

J.M. Cowley

X-ray measurement of order in single crystals of Cu3Au

J. Appl. Phys., 21 (1950), pp. 24-30, 10.1063/1.1699415
Google Scholar
[40]

Chen S., Aitken Z.H., Pattamatta S., Wu Z., Yu Z.G., Banerjee R., Srolovitz D.J., Liaw P.K., Zhang Y.-W.. Chemical-Affinity Disparity and Exclusivity Drive Atomic Segregation, Short-Range Ordering, and Cluster Formation in High-Entropy Alloys. Acta Materialia, 2021, **206**: 116638 (10 pages). 10.1016/j.actamat.2021.116638.
Google Scholar
[41]

Chen S., Aitken Z.H., Pattamatta S., Wu Z., Yu Z.G., Srolovitz D.J., Liaw P.K., Zhang Y.-W.. Simultaneously enhancing the ultimate strength and ductility of high-entropy alloys via short-range ordering. Nature Communications, 2021, **12**: 4953 (11 pages). 10.1038/s41467-021-25264-5.
Google Scholar
[42]

Qi Y., Chen X., Feng M.. Molecular dynamics-based analysis of the effect of voids and HCP-Phase inclusion on deformation of single-crystal CoCrFeMnNi high-entropy alloy. Materials Science and Engineering: A, 2020, **791**: 139444 (9 pages). 10.1016/j.msea.2020.139444.
Google Scholar
[43]

Xiao J., Deng C.. Martensite transformation induced superplasticity and strengthening in single crystalline CoNiCrFeMn high entropy alloy nanowires: A molecular dynamics study. Materials Science and Engineering: A, 2020, **793**: 139853 (9 pages). 10.1016/j.msea.2020.139853.
Google Scholar
[44]

Jarlöv A., Ji W., Zhu Z., Tian Y., Babicheva R., An. R, Seet L.S., Nai M.L.S., Zhou K.. Molecular dynamics study on the strengthening mechanisms of Cr–Fe–Co–Ni high-entropy alloys based on the generalized stacking fault

energy. Journal of Alloys and Compounds, 2022, **905**: 164137 (12 pages). 10.1016/j.jallcom.2022.164137.
Google Scholar
[45]

M. Rahm, R. Hoffmann, N.W. Ashcroft

Atomic and Ionic Radii of Elements 1–96

Chem. Eur. J., 22 (2016), pp. 14625-14632, 10.1002/chem.201602949
View in ScopusGoogle Scholar
[46]

Li L., Kamachali R.D., Li Z., Zhang Z.. Grain boundary energy effect on grain boundary segregation in an equiatomic high-entropy alloy. Physical Review Materials, 2020, **4**: 053603 (11 pages). 10.1103/PhysRevMaterials.4.053603.
Google Scholar
[47]

L. Zhang, C. Lu, K. Tieu

Atomistic Simulation of Tensile Deformation Behavior of Σ5 Tilt Grain Boundaries in Copper Bicrystal

Sci. Rep., 4 (1) (2014), 10.1038/srep05919
Google Scholar
[48]

H.R. Peng, Z.Y. Jian, C.X. Liu, L.K. Huang, Y.M. Ren, F. Liu

Uncovering the softening mechanism and exploring the strengthening strategies in extremely fine nanograined metals: A molecular dynamics study

J. Mater. Sci. Technol., 109 (2022), pp. 186-196, 10.1016/j.jmst.2021.08.078
View PDFView articleView in ScopusGoogle Scholar
[49]

Koju R.K., Mishin Y.. The Role of Grain Boundary Diffusion in the Solute Drag Effect. Nanomaterials, 2021, **11**: 2348 (21 pages). 10.3390/nano11092348.
Google Scholar
[50]

D. Zhou, O.M. Løvvik, K. Marthinsen, Y. Li

Segregation of Mg, Cu and their effects on the strength of Al Σ5 (210)[001] symmetrical tilt grain boundary

Acta Mater., 145 (2018), pp. 235-246, 10.1016/j.actamat.2017.12.023
Google Scholar
[51]

J. Li, X. Yang, P. Wang

Shear-coupled grain boundary migration in bicrystal Ni with metallic dopant segregation

J. Mater. Res., 36 (3) (2021), pp. 775-783, 10.1557/s43578-020-00030-3
View in ScopusGoogle Scholar
[52]

T.W. Heo, S. Bhattacharyya, L.-Q. Chen

A phase field study of strain energy effects on solute–grain boundary interactions

Acta Mater., 59 (2011), pp. 7800-7815, 10.1016/j.actamat.2011.08.045
View PDFView articleView in ScopusGoogle Scholar
[53]

Li R., Zhou J., Li Y., Liu Y., Zhao B., Ren F.. Grain boundary migration and Zener pinning in a nanocrystalline Cu–Ag alloy. Modelling and Simulation in Materials Science and Engineering, 2020, **28**: 065017 (15 pages). 10.1088/1361-651X/aba737.
Google Scholar
[54]

Z.W. Lu, B. Klein, A. Zunger

Spin-Polarization-Induced Structural Selectivity in Pd3X and Pt3X (X = 3d) Compounds

Phys. Rev. Lett., 75 (7) (1995), pp. 1320-1323, 10.1103/PhysRevLett.75.1320
View in ScopusGoogle Scholar
[55]

Zhu M., Wu P., Li Q., Xu B.. Vacancy-induced brittle to ductile transition of W-M co-doped Al3Ti (M=Si, Ge, Sn and Pb). Scientific Reports, 2017, **7**: 13964 (7 pages). 10.1038/s41598-017-14398-6.
Google Scholar
[56]

X. Gao, R. Hu, J. Yang

The effect of Ni3(Cr0.2W0.4Ti0.4) particles with DO22 structure on the deformation mode and mechanical properties of the aged Ni-Cr-W-Ti alloy

Scr. Mater., 153 (2018), pp. 44-48, 10.1016/j.scriptamat.2018.04.029
View PDFView articleView in ScopusGoogle Scholar
[57]

Shi Y., Guo C., Chen J., Xiao X., Huan H., Yang B.. Recrystallization behavior and mechanical properties of a Cu–15Ni–8Sn(P) alloy during prior deformation and aging treatment. Materials Science & Engineering: A, 2021, **826**: 142025 (16 pages). 10.1016/j.msea.2021.142025.
Google Scholar
[58]

Rahnama A., Kotadia H., Clark S., Janik V., Sridhar S.. Nano-mechanical properties of Fe-Mn-Al-C lightweight steels. Scientific Reports, 2018, **8**(1): 9065 (12 pages). 10.1038/s41598-018-27345-w.
Google Scholar
[59]

Lechermann F., Welsch F., Elsässer C., Ederer C., Fähnle M., Sanchez J.M., Meyer B.. Density-functional study of Fe3Al: LSDA versus GGA. Physical Review B, 2002, **65**: 132104 (4 pages). 10.1103/PhysRevB.65.132104.
Google Scholar
[60]

R. Feng, M.C. Gao, C. Zhang, W. Guo, J.D. Poplawsky, F. Zhang, J.A. Ha wk, J.C. Neuefeind, Y. Ren, P.K. Liaw

Phase stability and transformation in a light-weight high-entropy alloy

Acta Mater., 146 (2018), pp. 280-293, 10.1016/j.actamat.2017.12.061
View PDFView articleView in ScopusGoogle Scholar
[61]

I.S. Wani, T. Bhattacharjee, S. Sheikh, P.P. Bhattacharjee, S. Guo, N. Tsu ji

Tailoring nanostructures and mechanical properties of AlCoCrFeNi2.1 eutectic high entropy alloy using thermomechanical processing

Mater. Sci. Eng., A, 675 (2016), pp. 99-109, 10.1016/j.msea.2016.08.048
View PDFView articleView in ScopusGoogle Scholar
[62]

Dasari S., Jagetia A., Chang Y.-J., Soni V., Gwalani B., Gorsse S., Yeh A.-C., Banerjee R.. Engineering multi-scale B2 precipitation in a heterogeneous FCC based microstructure to enhance the mechanical properties of a Al0.5Co1.5CrFeNi1.5 high entropy alloy. Journal of Alloys and Compounds, 2020, **830**: 154707 (15 pages). 10.1016/j.jallcom.2020.154707.
Google Scholar
[63]

S. Wei, C.C. Tasan

Deformation faulting in a metastable CoCrNiW complex concentrated alloy: A case of negative intrinsic stacking fault energy?

Acta Mater., 200 (2020), pp. 992-1007, 10.1016/j.actamat.2020.09.056
View PDFView articleView in ScopusGoogle Scholar
[64]

Su Y., Xu S., Beyerlein I.J.. Density functional theory calculations of generalized stacking fault energy surfaces for eight face-centered cubic transition metals. Journal of Applied Physics, 2019, **126**: 105112 (12 pages). 10.1063/1.5115282.
Google Scholar
[65]

Li Q.-J., Sheng H., Ma E. Strengthening in multi-principal element alloys with local-chemical-order roughened dislocation pathways. Nature Communications, 2019, **10**: 3563 (11 pages). 10.1038/s41467-019-11464-7.
Google Scholar